RSC Advances

PAPER

View Article Online
View Journal | View Issue



Cite this: *RSC Adv.*, 2025, **15**, 47171

# Sustainable novel chitosan sulfonamides conjugated with a phthalazine derivative for enhanced corrosion inhibition in acidic environments

Hamdy Khamees Thabet,[a] Moustafa S. Abusaif, *[bc] Amr Gangan,*[b] Ahmed E. Hassan,[d] Yousry A. Ammar, [b] Sobhi M. Gomha,[e] Magdi E. A. Zaki[f] and Ahmed Ragab [bg]

Chitosan, a biopolymer material, has shown great promise as a biodegradable corrosion inhibitor. Herein, this research details the synthesis of new chitosan sulfonamide conjugates by coupling chitosan with 1,4-phthalazinedione sulfonyl chloride (DEPS) at various molar ratios to create enhanced, eco-friendly corrosion inhibitors (CHDEPS1-3). The modifications increased the biopolymer's crystallinity, peaking at 79.80% for CHDEPS3 compared to 64% for native chitosan. The protective performance of the inhibitors on carbon steel in an acidic medium was assessed using electrochemical tests, weight loss measurements, and surface characterization. The findings were highly positive, especially with CHDEPS3 demonstrating a superior inhibition efficiency of 95.38% at a concentration of 400 ppm. Atomic Force Microscopy (AFM) confirmed the formation of a protective adsorbed layer, which reduced the steel's average surface roughness from 852.05 nm to just 36.78 nm. Theoretical analysis, including quantum chemical calculations, molecular dynamics, and Monte Carlo simulations, elucidated the adsorption mechanism. The potentiodynamic polarization data and significantly negative Gibbs free energy values ($\Delta G$: −30.04 to −35.75 kJ mol$^{-1}$) confirmed a spontaneous, mixed physical–chemical adsorption process, occurring *via* the formation of Fe–N and Fe–O bonds at the steel/solution interface. The study concludes that the insertion of the phthalazine moiety successfully enhanced the inhibitor's electrostatic effect, hydrophobicity, and overall efficiency by promoting robust interfacial adsorption.

Received 29th August 2025
Accepted 21st November 2025

DOI: 10.1039/d5ra06483j

rsc.li/rsc-advances



## 1 Introduction

Corrosion inhibitor materials play a crucial role in extending the durability of engineering materials when exposed to challenging environments. Their function is to safeguard embedded steel within reinforcements by blocking chlorides and various corrosive agents, thus preventing damage associated with corrosion. In addition, inhibitors may be added to coating formulas applied to steel surfaces, resulting in a compact protective layer that separates the metal from corrosive conditions and slows the corrosion process.[1] Consequently, research continues to identify compounds and complexes capable of forming compact, protective films or layers on steel to mitigate corrosion-induced degradation across various corrosive environments.[2] Notwithstanding the advantageous characteristics of steel, like its natural abundance, affordability, and durability, it faces considerable corrosion issues in many situations. This restriction encompasses vulnerability to corrosion, a characteristic that intensifies in an acidic environment.[3,4] There have been attempts to preserve steel using inorganic corrosion inhibitors based on ceria, phosphates, and chromates,[5,6] but these compounds have serious hazardous effects. Consequently, authorities limit their use.[7] As a result, scholars have explored organic corrosion inhibitors such as derivatives of imidazole, thiazoles, and hydrazine Schiff bases, among others, as less toxic alternatives capable of forming highly protective films on metals through donor–acceptor and/or electrostatic

[a]*Center for Scientific Research and Entrepreneurship, Northern Border University, Arar 73213, Saudi Arabia*

[b]*Department of Chemistry, Faculty of Science (Boys), Al-Azhar University, 11884 Nasr City, Cairo, Egypt. E-mail: mostafahozaifa317@azhar.edu.eg; amr_gangan@azhar.edu.eg*

[c]*Department for Synthesis and Characterization of Polymers, Polymer Institute of the Slovak Academy of Sciences, Dúbravská Cesta 9, 845 41 Bratislava, Slovak Republic*

[d]*Interdisciplinary Research Center for Hydrogen Technologies and Carbon Management (IRC-HTCM), King Fahd University of Petroleum & Minerals, Dhahran 31261, Saudi Arabia*

[e]*Department of Chemistry, Faculty of Science, Islamic University of Madinah, Madinah 42351, Saudi Arabia*

[f]*Department of Chemistry, College of Science, Imam Mohammad Ibn Saud Islamic University (IMSIU), 11623 Riyadh, Kingdom of Saudi Arabia*

[g]*Chemistry Department, Faculty of Science, Galala University, Galala City, Suez 43511, Egypt*

mechanisms.[8–11] This insight has significantly contributed to the development of several less harmful corrosion inhibitors. Generally, chemical inhibitors have shown efficacy in forming a protective barrier on metallic surfaces, thus preventing interaction between the metals and corrosive agents.

The growing recognition of sustainable ecosystem development has recently led to a significant interest in eco-friendly corrosion inhibitors.[12,13] Natural polymers, such as chitosan, starch, and guar gum, represent a category of environmentally friendly compounds that hold promise as efficient and eco-friendly corrosion inhibitors. The presence of oxygen atoms in their molecular structures allows them to serve as active sites for adsorption on the surface of carbon steel.[14–16] Corrosion inhibitors derived from biomass, including natural polymers, are inexpensive, biodegradable, and relatively safe for humans and the environment.[17] Therefore, the corrosion resistance of this material is a critical issue in both industrial applications and scientific research. They hold particular significance in acidic environments, where the corrosion process may manifest with heightened aggression.[18–20] Especially, chitosan and its derivatives have garnered greater interest among these natural polymers due to the significant quantity of hydroxyl (OH) and amino functions ($NH_2$), which makes them easier to adsorb on the surfaces of steel. Indeed, chitosan enables the production of ceramic composite coatings at ambient temperatures, whereas ceramic deposits typically require elevated temperatures to form a thick and adherent coating.[21,22] Chitosan dissolves in most weak organic acids, including formic and acetic acid, but does not dissolve in water or neutral pH.[23] This makes it challenging to find an effective coating solution for chitosan. Additionally, the inhibitory effectiveness of chitosan is not excellent in most environments.[24] Therefore, the previous problem can be solved by designing chemically modified chitosan that incorporates organic functional groups *via* either the amino group or hydroxyl group, which enhances the inhibition efficiency. This modification would be beneficial if the researcher selected suitable organic materials with acceptable corrosion inhibition.[25,26] Menaka and Subhashini investigated the inhibition potential of chitosan thiophene carboxaldehyde Schiff base for mild steel (MS) in a 1.0 M HCl solution. They employed a comprehensive set of methods, including weight loss (WL), electrochemical techniques (EIS and PDP), and surface characterization (SEM, EDX, and AFM). The weight loss study, conducted at various temperatures and concentrations, showed that modified chitosan Schiff base demonstrated its optimal inhibition performance of 86.94% at a concentration of 1500 ppm and a temperature of 333 K.[27] In a study by Haque and coworkers, three chitosan Schiff Bases (CSBs) were synthesized and characterized to test their effectiveness in corrosion protection. Compounds chitosan-benzaldehyde (CSB-1), chitosan-4-(dimethylamino)benzaldehyde (CSB-2), and chitosan-4-hydroxy-3-methoxybenzaldehyde (CSB-3), were evaluated on mild steel in a 1.0 M HCl solution. A weight loss study conducted at concentrations ranging from 50 to 150 ppm indicated that the protection potential improved as the concentration increased. At an optimum concentration of 100 ppm, the inhibition efficiencies followed the sequence: CSB-3 (91.43%) > CSB-2 (89.87%) > CSB-1 (88.63%). This order of efficiency was further validated by EIS and PDP electrochemical studies.[28] Ansari*et al.* synthesized and studied a salicylaldehyde-chitosan cationic surfactant Schiff Base (SCSB) as an eco-friendly corrosion inhibitor for steel. The experiments were conducted in a harsh environment of 3.5% NaCl saturated with carbon dioxide at 65 °C. The results showed that SCSB functions *via* a mixed-type adsorption mechanism, achieving a high efficiency of 95.2% at a concentration of 150 mg $L^{-1}$. This reduced the corrosion rate to 0.444 mm $y^{-1}$. Furthermore, impedance measurements indicated that the corrosion inhibition process is kinetically controlled.[29]

Small organic compounds rich in heteroatoms, such as sulfur, nitrogen, and oxygen, typically provide the best corrosion protection. These compounds function by adsorbing onto the metal surface, a process that displaces existing water molecules. This adsorption creates a dense, protective barrier that stifles corrosion by impeding the anodic, cathodic, or mixed electrochemical reactions.[30] As a result, phthalazine has a bicyclic structure that includes fused benzene and pyridazine rings. This arrangement offers a stable framework that can be readily adjusted to improve environmental applications.[31,32] Abd El-Maksoud *et al.* confirmed the effectiveness of phthalazine derivatives as corrosion inhibitors for copper in 1 M $H_2SO_4$ through electrochemical polarization and weight loss techniques.[32] Research has focused on the evolution of this inhibitory effect, linking it directly to the specific constitution of the derivatives. This clear structure–activity relationship presents an interesting challenge for the development of new, efficient synthetic methods for phthalazine ring fragments, leading to numerous reported preparation strategies.[33] In addition, Hemdan and his co-workers successfully synthesized 11 new phthalazine derivatives based on the triazole moiety and investigated them as inhibitors of the corrosion of steel immersed in 5.0 M HCl solutions.[34] The corrosion inhibition tendency of the synthesized phthalazines achieved a high efficiency of 93.4%.

On the other hand, density functional theory (DFT) has become a widely used computational tool for corrosion scientists, providing a practical approach to studying the molecular-level interactions between an inhibitor and a metal. Such quantum chemical computations are frequently used to analyze the molecular electronic structures of organic inhibitors using various quantum chemical descriptors. The field has since advanced to modeling the entire inhibitor-metal surface system. This modern approach calculates total interaction energies, including both covalent and non-covalent forces, to provide critical physical insights into the underlying mechanisms of corrosion inhibition.[35] Molecular dynamics (MD) simulation is a powerful computational tool used to understand corrosion inhibition at the atomic level. It functions as a "computational microscope," allowing researchers to visualize and quantify the interactions between inhibitor molecules, a metal surface, and a corrosive environment (like an acid solution).[36]

So, this study details the design and synthesis of an eco-friendly, sustainable modified chitosan sulfonamide that

 

incorporates a phthalazine nucleus. The chemical structure of the newly synthesized material was analyzed through IR and NMR spectroscopy, as well as CHN elemental analysis. This study systematically examines the enhancement of corrosion inhibition properties of native chitosan through the incorporation of phthalazine nuclei. The effectiveness of synthetic materials in inhibiting corrosion is assessed using a low-carbon steel sample immersed in a 1.0 M HCl solution, employing methodologies that include AC impedance, potentiodynamic polarization, and weight loss analysis. The theoretical calculations, encompassing the adsorption model, inhibition mechanism, DFT calculations, and Monte Carlo (MC)/molecular dynamics (MD) simulations, have been analyzed to validate the practical data acquired. Fortunately, this work presents a promising route to enhance the anticorrosion properties of materials by incorporating the phthalazine moiety into the chitosan backbone. This method has not been previously documented. The author also hopes to demonstrate the promising future of modified natural polymers in various environmental applications through this chemical modification and targeted use.

# 2 Experimental section

## 2.1. Materials

Chitosan powder was purchased from Qingdao Yunzhou Biochemistry Co., Ltd., China, with an 85% deacetylation degree and an average molecular weight of $4 \times 10^4$ g mol$^{-1}$. Phthalic anhydride (PA; purity > 99%), 1,2-diethylhydrazine (DH; purity > 98%), *N*-ethyl-*N*,*N*-diisopropylamine (purity > 99%), and chlorosulfonic acid ($ClSO_3H$; purity > 99%) were purchased from Sigma–Aldrich Co., Germany. Additionally, the solvents used, including absolute ethanol (EtOH, purity ≥ 99.99%), methylene chloride ($CH_2Cl_2$, purity ≥ 98.00%), and dimethyl sulfoxide (DMSO, purity ≥ 99.99%), were purchased from El-Nasr Company, Egypt.

A carbon steel sample (CS) was obtained from the Central Metallurgical Research Institute in Egypt and was shaped into disc-shaped steel samples (10 mm in diameter). These samples were polished using silicon carbide emery papers of different grades (60, 80, 120, 400, 800, 1000, and 2000) to achieve a smooth surface. After that, the samples were washed in acetone and dried at room temperature.

FOUNDRY-MASTER Optical Emission Spectrometer analyzed the carbon steel sample. The composition of it (in wt%) is as follows: 0.271% C, 0.214% Si, 0.829% Mn, 0.0305% P, 0.0156% S, 0.0122% Cr, 0.0187% Ni, 0.0033% Al, 0.0041% Co, 0.0071% Cu, 0.0001% Ti, 0.0028% V, 0.0095% W, 0.0095% Pb, 0.0108% As, 0.0003% B and 98.57% Fe.

## 2.2. Chemical synthesis of target materials

**2.2.1. Chemical synthesis of 2,3-diethyl-2,3-dihydrophthalazine-1,4-dione (DEP).** The target organic phthalazine material DEP was synthesized according to the method reported by Nielsen *et al.*[37] It was obtained as a colorless solid with the same reported melting point, mp 156–158 °C, with an acceptable yield of 74%.

**2.2.2. Chemical synthesis of 2,3-diethyl-1,4-dioxo-1,2,3,4-tetrahydrophthalazine-6-sulfonyl chloride (DEPS).** Highly dry DEP material (11.46 mmol, 2.50 g) was gradually added to chlorosulfonic acid ($SO_2(OH)Cl$) (22.92 mmol, 2.67 g) at room temperature, and the resultant mixture was stirred for 4 h at constant temperature, 60 °C. The mixture was chilled in an ice bath and poured into chopped ice with continuous stirring until the required white solid precipitated. The solid product underwent filtration and was then washed three times with cold water before being air-dried. The solid was recrystallized from benzene, yielding white needles of sulfonyl chloride derivatives DEP.

Pale white color; yield: 89%; mp: 135–137 °C; IR (KBr): $\nu_{max}$ = 2988, 2939, 2872 (CH-aliph.), 1722 (CO), 1578 (C=C), 1331, 1147 ($SO_2$); $^1$H NMR (ppm) $\delta$ 1.26 (6H, s, $2CH_3$), 3.25 (4H, s, $2CH_2$), 7.60 (1H, d, $J$ = 6.8, Ph-H), 8.02 (1H, d, $J$ = 8.0, Ph-H), 8.13 (1H, s, Ph-H); $^{13}$C NMR ($\delta$, ppm) 19.02 (C, $2CH_3$), 48.28 (C, $2CH_2$), 117.66 (C, arom.), 119.59 (C, arom.), 127.58 (C, arom.), 129.84 (C, arom.), 131.40 (C, arom.), 139.43 (C, arom.), 161.53 (2CO).

**2.2.3. Chemical synthesis of functionalized chitosan-phthalazine sulfonamide (CHDEPS1-3).** To a solution of the natural polymer, chitosan CH (0.55 mmol, 1.0 g) and the corresponding phthalazine sulfonyl chloride derivative DEPS in anhydrous methylene chloride containing triethylamine as a base catalyst. The reaction mixture was stirred at room temperature for 16 h until the amount of sulfonyl chloride consumed (monitoring with TLC). The new solid product was filtered out, washed with ethanol three times and dried. A subsequent step in the purification process included washing with acetone to eliminate any remaining unreacted sulfonyl chloride. To investigate the influence of reactant stoichiometry, a series of chitosan sulfonamide was synthesized by varying the ratio of DEPS to dry chitosan. The reactions were performed using 0.25 : 1, 0.5 : 1, and 1 : 1 mmol of DEPS per gram of chitosan. The complete synthetic pathway for the intermediate and target compounds is depicted in Scheme 1, and the corresponding sample codes are listed in Table 1.

## 2.3. Electrochemical measurements

The AC impedance technique EIS was used to measure electrochemical experiments. The electrochemical experiments were conducted using a Potentiostat/Galvanostat/ZRA analyzer (GAMRY Reference 3000), with a conventional three-electrode setup comprising a saturated calomel reference electrode (SCE) and a platinum grid as the counter electrode. The surface area of the working electrode was 1 cm$^2$.

Potentiodynamic polarization tests were performed by scanning the applied potential from −0.3 to 1 V at a scan rate of 2 mV s$^{-1}$. The corrosion rate $k_{corr}$ in (mmpy) was obtained from the $I_{corr}$ values by the following equation.

$$\text{Corrosion rate} = 3.27 \times 10^{-3} \times I_{corr}\ (\mu\text{A cm}^{-2}) \times \frac{\text{Eq. wt}}{\text{density}} \quad (1)$$

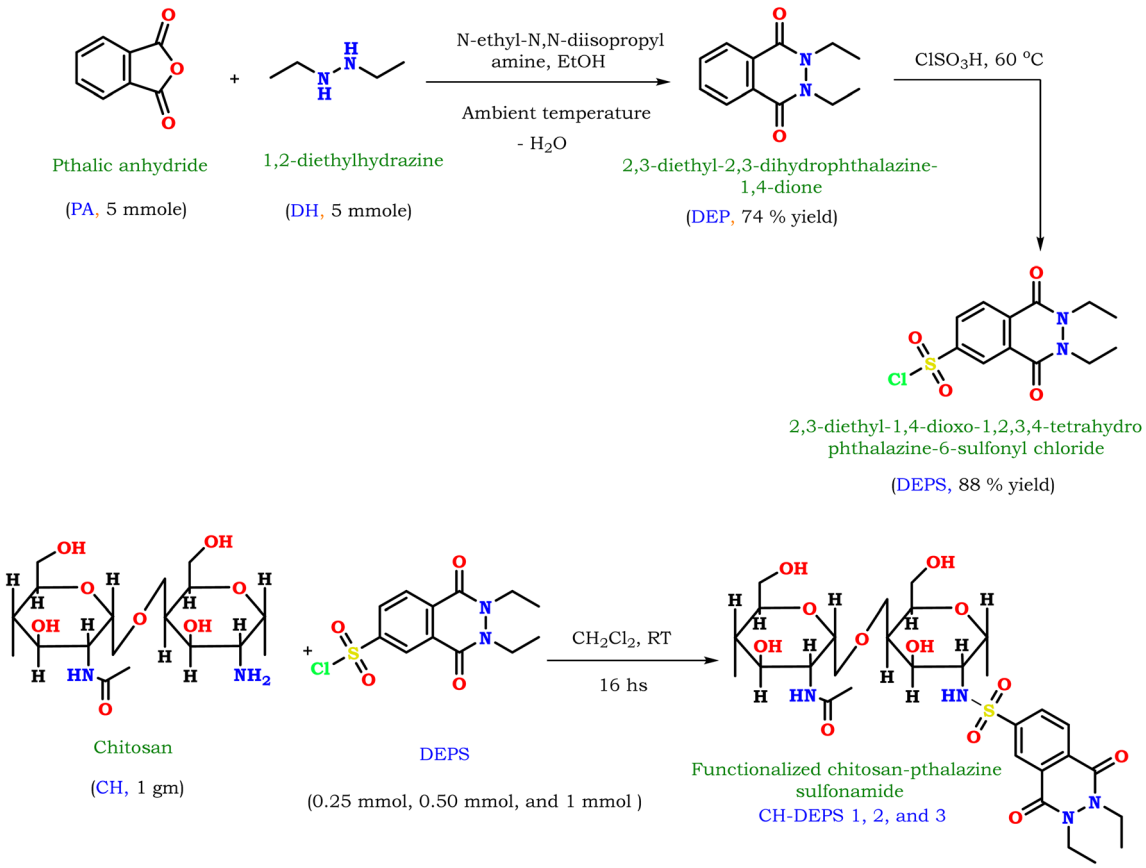


Scheme 1 Synthetic routes of substituted phthalazine sulfonyl chloride (DEPS), and their functionalized chitosan sulfonamides (CH-DEPS).

Table 1 Sample codes of chitosan-sulfonamide derivative depend on DEPS : chitosan ratios

| Chitosan-sulfonamide code | Phthalazine sulfonyl chloride derivative (DEPS) | Chitosan (CH) |
|---|---|---|
| CHDEPS1 | 0.25 mmol | 0.55 mmol, 1.0 g |
| CHDEPS2 | 0.5 mmol | 0.55 mmol, 1.0 g |
| CHDEPS3 | 1 mmol | 0.55 mmol, 1.0 g |

where $I_{corr}$ is the corrosion current density, Eq. wt is the equivalent weight of the carbon steel (27.93 g), and its density is 7.86 g $cm^{-3}$. The inhibition efficiency ($\eta_{pol}$) was calculated from the potentiodynamic parameter.

$$\eta_{pol} = \left[1 - \frac{I_{corr}}{I^{\circ}_{corr}}\right] \times 100 \quad (2)$$

where $I^{\circ}_{corr}$ and $I_{corr}$ are the corrosion current densities of untreated (blank) and treated samples, respectively.

Electrochemical impedance spectroscopy (EIS) was performed by applying an AC excitation of 10 mV amplitude (peak-to-peak) of sinusoidal voltage in the frequency range from 100 kHz to 10 mHz at open-circuit potential (OCP). Impedance data were modeled using Gamry Echem Analyst software to choose proper electrochemical equivalent circuits and calculate EIS parameters. Also, the inhibition efficiency ($\eta_{EIS}$) was calculated using the following equation.[38]

$$\eta_{EIS} = \left[1 - \frac{R^{\circ}_{ct}}{R_{ct}}\right] \times 100 \quad (3)$$

where $R^{\circ}_{ct}$ and $R_{ct}$ are the charge transfer resistance of untreated (blank) and treated steel samples, respectively. The electrochemical measurements of treated steel were carried out in a 1.0 M HCl solution using hydrochloric acid (37%).

### 2.4. Weight loss measurements

Samples were originally weighed using an electronic balance. Weighed samples were immersed in 100 mL of 1.0 M HCl with varying doses of 50, 100, 200, and 400 ppm of new inhibitors (CH, CHDEPS1, CHDEPS2, and CHDEPS3) at 298–353 K. Following the adjustment of temperature and the specified immersion duration, the specimens were removed from the test solution, dried in a moisture-free desiccator, and subsequently re-weighed using a sensitive analytical balance, Model FA 2104A (capacity: 210 g, readability: 0.1 mg). The difference in weight is considered as weight loss in each instance. The corrosion rates were determined using the given formula:

$$CR = \Delta W \times 534/Atd \quad (4)$$

CR represents the corrosion rate measured in mg $cm^{-2}$ $h^{-1}$. $\Delta W$ denotes the change in sample weight, expressed in grams (g), which is determined by the difference before and after immersion in the test solution. $A$ indicates the surface area of the steel samples, measured in square centimeters ($cm^2$). The variable $t$ refers to the exposure time, recorded in hours (h), while $d$ signifies the density of CS, measured in grams per cubic centimeter (mg $cm^{-3}$).

A calculation was made using the provided equation to determine the degree of surface covering ($\theta$):

$$\theta = \frac{W_0 - W_i}{W_0} \quad (5)$$

$W_i$ and $W_0$ represent the weight loss values of steel samples in inhibited and uninhibited solutions, respectively. Also, the inhibition efficiency was determined using the following equation:[39]

$$IE\% = \theta \times 100 \quad (6)$$

### 2.5. Surface morphological analysis

The low-carbon steel sample was first immersed in a 1.0 M HCl solution, both in the absence and presence of varying concentrations (50–400 ppm) of each target inhibitor, at 298 K. After 24 hours, the samples were removed from the test solution, washed with bi-distilled water, and dried. SEM-EDX investigation was performed using an EDX device attached to a SEM Model Quanta 250 FEG with an accelerating voltage of 30 V.

### 2.6. Computational methods

Density functional theory (DFT) calculations were performed using Gaussian 16 software.[40] Initial geometries of chitosan (CH) and its derivative (CH-DEPS) were optimized using the B3LYP/6-31G*.[41] The global reactivity parameters, including bandgap energy ($\Delta E$), electron affinity ($A$), ionization potential ($I$), chemical hardness ($\eta$), softness ($\sigma$), electronegativity ($\chi$), electrophilicity ($\omega$), and chemical potential ($\mu$), were obtained from HOMO/LUMO energy Eigenvalues.[42] The TD-DFT computations were performed to simulate the UV-Vis spectra and predict the electronic excitation energies, wavelengths ($\lambda_{max}$), orbital contributions, and oscillator strengths ($f$) for the lowest 10 singlet transitions.[43] Molecular dynamics (MD) and Monte Carlo (MC) simulations were employed to investigate the interactions between metal surfaces and inhibitor molecules in simulated acidic media (300$H_2O$, 20$H_3O^+$, and 20$Cl^-$). MC and MD simulations were conducted using the Adsorption Locator and Forcite modules in Materials Studio software.[44] The Fe(110) surface was represented as a periodic slab of four atomic layers (15 × 15 Å). The system consisted of the Fe(110) surface, an inhibitor molecule, and a 30 Å vacuum region. The adsorption energy ($E_{ads}$), defined as the negative of inhibitor–surface interaction energy, was obtained from these simulations, reflecting adsorption strength. MD simulations investigated the dynamic stability of the inhibitor on Fe(110) surfaces at a temperature of 298 K. The COMPASS III force field with a 1 fs integration timestep was applied. Simulations involved a 50 ps equilibration followed by a 500 ps production run (*NVT* ensemble). Analysis focused on inhibitor adsorption stability, inhibitor–surface interaction energies, and radial distribution functions to evaluate chemisorption behavior and adsorption strength.

## 3 Results and discussion

### 3.1. Chemical synthesis of the functionalized modified polymer

In the present work, amphiphilic modified chitosan sulfonamide materials, CHDEPS, were designed and synthesized with the expectation as promising corrosion inhibitors. The target CH-DEPS1, CHDEPS2, and CHDEPS3 materials (Functionalized natural polymers) were created by introducing the phthalazine moiety (with different molar ratios) into the chitosan polymer *via* a sulfonamide function, as presented in Scheme 1. First, a newly phthalazine sulfonyl chloride derivative, 2,3-diethyl-1,4-dioxo-1,2,3,4-tetrahydrophthalazine-6-sulfonyl chloride (DEPS), was successfully synthesized with high yield *via* two-step process. First step involved base-catalyzed condensation reaction between phthalic anhydride (PA), and 1,2-diethylhydrazine (DA), where the base catalyst promotes the nucleophilicity of secondary amine, producing the intermediate, 2,3-diethyl-2,3-dihydrophthalazine-1,4-dione (DEP). In addition, the secondary amine of 1,2-diethylhydrazine (DA) is the nucleophile in this reaction. In addition, the base is reconstituted during the cyclization phase.[37,45] Second, the intermediate was reacted with chlorosulfonic acid under reflux conditions *via* electrophilic substitution reaction, producing the 2,3-diethyl-1,4-dioxo-1,2,3,4-tetrahydrophthalazine-6-sulfonyl chloride (DEPS). Chlorosulfonic acid is a powerful electrophile since the sulfur atom draws electron density from the phthalazine ring, preparing a phthalazine-sulfonyl chloride intermediate.[46] Finally, the new sulfonyl chloride DEPS was allowed to react with chitosan *via* nucleophilic acyl substitution reaction, producing the modified non-ionic functionalized polymer, chitosan-DEPS sulfonamide. The chemical structure of the phthalazine sulfonyl chloride DEPS and modified chitosan sulfonamide CHDEPS was elucidated using significant spectral data and analytical techniques.

### 3.2. Evaluation of the degree of substitution using ion exchange capacity

Ion exchange capacity (IEC) examinations may indicate the formation of new sulfonamide functions *via* the aliphatic amine group ($NH_2$) in the chitosan structure. Thus, the IEC findings for CH recorded the most elevated value of 11.92 ± 0.83 $m_{eq}$ $g^{-1}$. By introducing the organic material DEPS *via* a sulfonamide chemical function, the IEC value began to decrease as the concentration of organic material increased. Notably, the IEC findings recorded reduced values of 10.19 ± 0.54, 8.12 ± 0.43, and 4.13 ± 0.39 $m_{eq}$ $g^{-1}$ for the CH-DEPS1, CH-DEPS2, and CH-

DEPS3 samples, respectively. Furthermore, the observed decline can be attributed to the interaction of the aliphatic amine in the CH backbone with the sulfonyl chloride derivative DEPS during the process of sulfonamide formation. Additionally, the nitrogen atoms in the sulfonamide function ($SO_2$–NH) did not affect the ion exchange capacity, as they are not ionizable under the examined conditions. Despite nitrogen atoms linked to the $SO_2$ group in the phthalazine moiety, these nitrogen atoms do

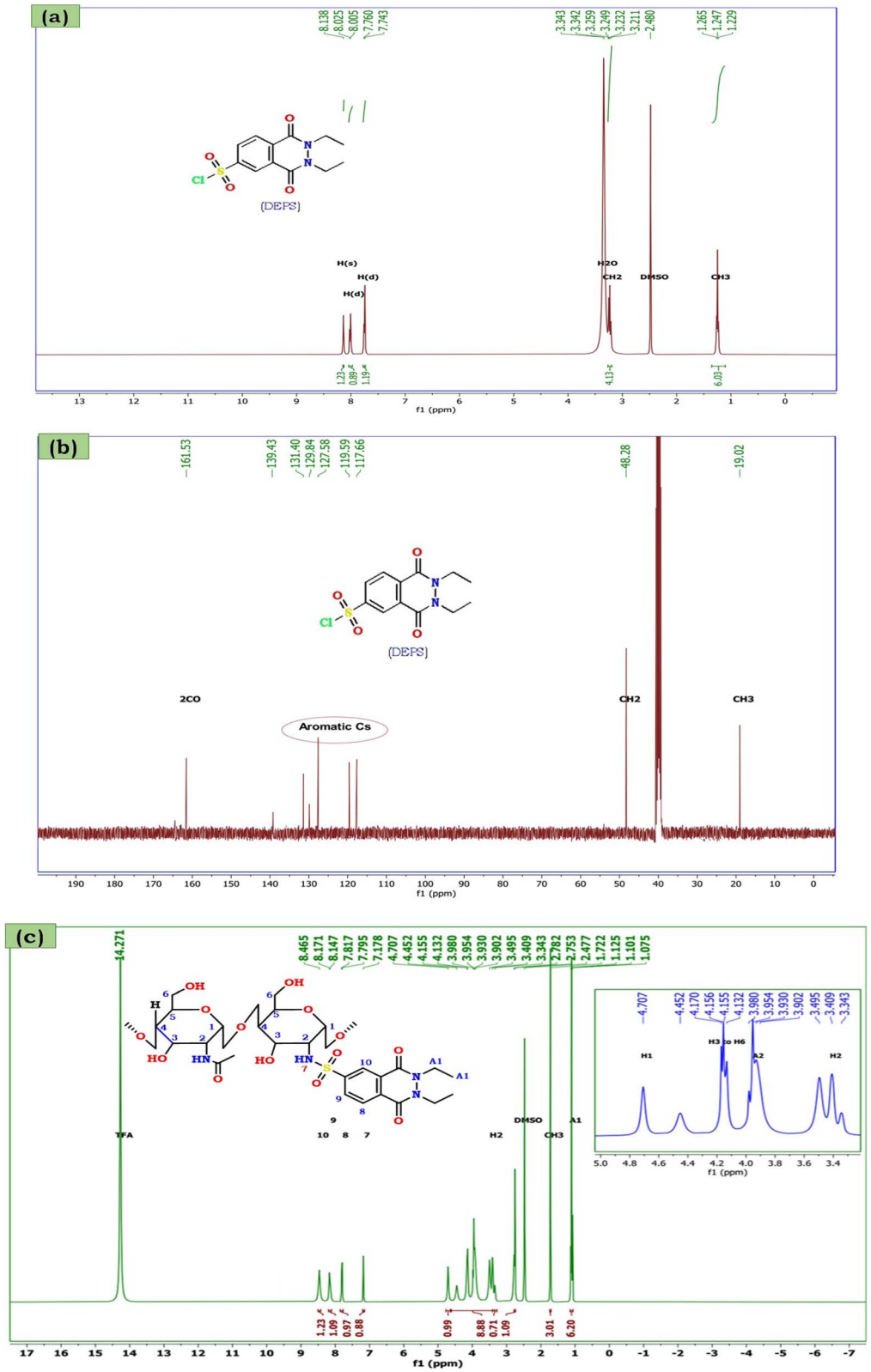


Fig. 1 $^{1}$H NMR & $^{13}$C NMR spectrum of DEPS (a), (b) respectively, and $^{1}$H NMR spectrum of CH-DEPS (c).

not act as a free basic secondary amine. Consequently, under the experimental conditions (utilizing 0.1 M $H_2SO_4$), the nitrogen remains unprotonated and does not substantially influence the IEC, as it's considered acidic NH is not basic. The alterations in IEC are, therefore, mainly ascribed to the formation of the target function rather than to the protonation of the nitrogen. The measurements of ion exchange capacity (IEC) showed a strong correlation with the observed degree of substitution.

### 3.3. Instrumental characterization

**3.3.1. NMR spectral characterization.** The NMR spectrum of the newly synthesized materials, DEPS and their modified counterparts, CHDEPS, was performed to elucidate the proposed chemical structure; furthermore, the results are illustrated in Fig. 1. First, the $^1$H NMR spectrum of the newly synthesized organic material DEPS, presented in Fig. 1a, confirmed the existence of aliphatic and aromatic protons. Specifically, Signals associated with diethyl parts (N–$CH_2CH_3$) were observed at $\delta$ 1.26 and 3.25 ppm, with triplet ($J$ = 5.2 Hz) and quartet ($J$ = 4.0 Hz) splitting, respectively, revealing the presence of $CH_3$ and $CH_2$ groups. Notable signals in the chart correspond to aromatic protons, observed as two doublet signals at $\delta$ 7.60 and 8.02 ppm, with coupling constants $J$ = 6.8 and 8.0 Hz, respectively, due to the $H_7$ and $H_8$ protons of the phthalazine derivative. In addition, a singlet signal owing to the H5 protons of the phthalazine ring was observed at $\delta$ 8.13 ppm.[47] Second, the $^{13}$C NMR data of the same compound elucidated its chemical structure, which is displayed in Fig. 3b. By screening the chart, four significant signals at $\delta$ 19.02, 48.28, 139.43, and 163.53 ppm are observed, corresponding to the carbon of the *N*-ethyl carbons, the carbon attached to the $SO_2$ group, and the two carbonyls of the lactam function, respectively. In addition, five singlet signals equivalent to five aromatic carbons were observed at $\delta$ 117.66, 119.59, 127.58, 129.84, and 131.40 ppm.

Subsequently, Fig. 1c presents the $^1$H NMR of the modified polymer material CHDEPS, which confirms the successful

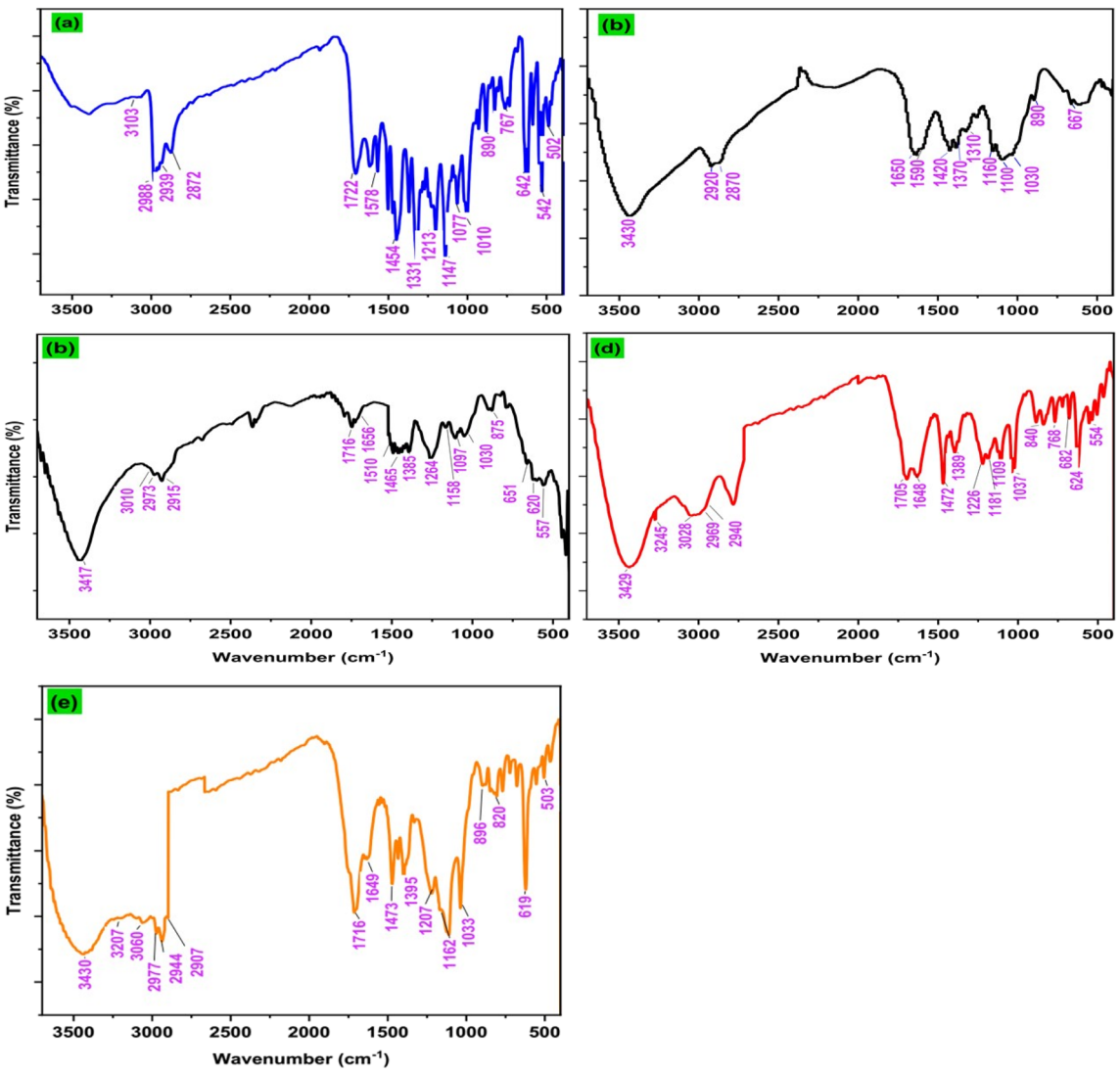


Fig. 2 FTIR spectral chart of (a) DEPS, (b) CH, (c) CH-DEPS1, (d) CH-DEPS2, and (e) CH-DEPS3.

reaction between chitosan CH and phthalazine sulfonyl chloride DEPS. Additionally, the $^1$H NMR spectra of the CHDEPS displayed the characteristic resonance signals of chitosan, along with the signal of the organic material, exhibiting some shifts due to the formation of a sulfonamide interaction. By screening the chart, a singlet signal appeared at $\delta$ 7.17 ppm, related to the NH proton of the newly formed sulfonamide function, which is more indicative of a successfully formed chemical linkage between chitosan and the organic material. Also, the chart revealed the main resonance signals of chitosan structure, as well as the signals of the organic material, DEPS (Fig. 1c).

**3.3.2. FT-IR spectral characterization.** FT-IR spectra were used to identify significant functional groups, confirming the chemical structure of the organic material DEPS and the modified chitosan sulfonamide. The corresponding charts are displayed in Fig. 2. First, Fig. 2a displayed the FT-IR spectrum of the phthalazine sulfonyl chloride derivative DSPS. Significant absorption bands at $\nu$ 3103, 2988, 2939, and 2872 cm$^{-1}$ are related to the sp$^2$-CH and sp$^3$-CH, respectively. Moreover, a distinguished peak at 1722 cm$^{-1}$, owing to the C=O bond of the lactam group, as well as a peak at 1454 cm$^{-1}$ corresponding to the C=C bond, beside bands observed at $\nu$ 1331 and 1147 cm$^{-1}$, related to the $SO_2$ function.[35,48] Continuously, the IR spectrum of pristine chitosan CH was displayed in Fig. 2b. A broad absorption frequency was detected at 3430 cm$^{-1}$, due to the stretching of the OH and $NH_2$ functions participating in a hydrogen bond. Weak absorption frequencies displayed at $\nu$ 2920 and 2870 cm$^{-1}$, related to the asymmetric vibrations of sp$^3$-CH. Next, the absorption peak at $\nu$ 1650 cm$^{-1}$ corresponds to the carbonyl bond of the residual acetamide group (NH–$COCH_3$), while the peak at 1590 cm$^{-1}$ is due to the N–H bending. Additionally, other peaks associated with $CH_3$ and $CH_2$ bending were detected at 1420 and 1370 cm$^{-1}$. The intense

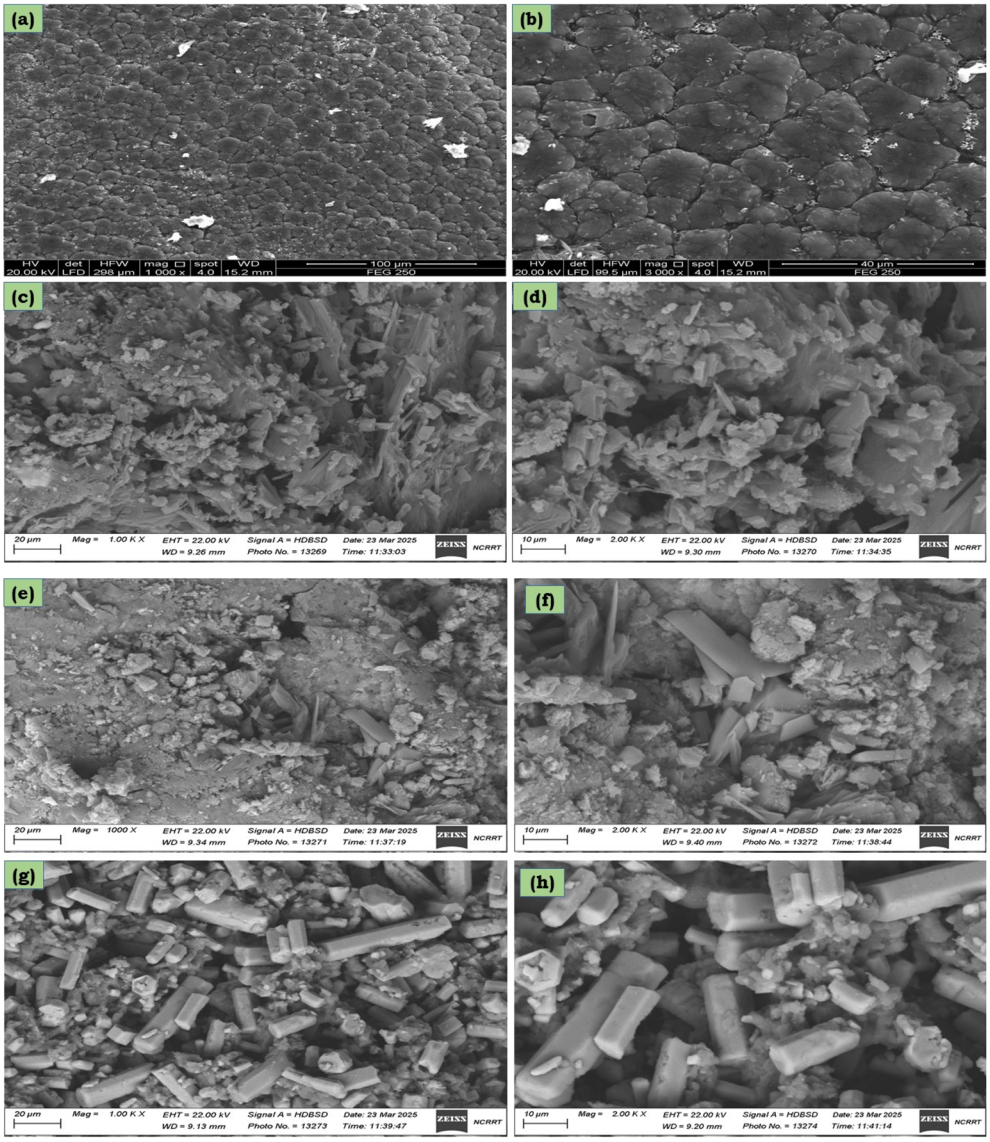


Fig. 3 SEM images of synthesized samples at different magnifications: (a) CH at 1000×, (b) CH at 3000×, (c) CH-DEPS 1 at 1000×, (d) CH-DEPS 1 at 2000×, (e) CH-DEPS 2 at 1000×, (f) CH-DEPS 2 at 2000×, (g) CH-DEPS 3 at 1000×, and (h) CH-DEPS 3 at 2000×.

absorption bands at $\nu$ 1160 $cm^{-1}$ were attributed to the asymmetric ether group (C–O–C), which bridges the glycoside rings. Peaks at 1100 and 1030 $cm^{-1}$ confirmed the presence of the C–O stretching group. Lastly, the C–H bending taking place outside the plane of the hexose ring was displayed at $\nu$ 890 $cm^{-1}$.[49]

Nevertheless, by the formation of chitosan-phthalazine sulfonamide, the broad peak detected between 3430 and 3200 $cm^{-1}$ was reduced from CHDEPS1 to CHDEPS3 because of the increase in the ratio of organic material (DEPS) due to the consumption of amino groups in chitosan (Fig. 2c–e). Also, the appearance of a new absorption peak at $\upsilon$ 3245–3207 $cm^{-1}$ indicated the establishment of the NH group of the new sulfonamide function ($SO_2$–NH), and the intensity of the peak increased by increasing the amount of organic material from CHDEPS1 to CHDEPS3 (Fig. 2c–e). Furthermore, the absorption frequencies observed at $\upsilon$ 3060, 2977, 2944, and 2907 $cm^{-1}$ are associated with the aromatic-CH of phthalazine derivative and aliphatic-CH of chitosan and phthalazine moiety, respectively. The band observed at around 1716 $cm^{-1}$ is due to the carbonyl bond of the lactam function in the phthalazine derivative. The intensity of the peak is heightened according to the sequence of CHDEPS3 > CHDEPS2 > CHDEPS1 samples, as a result of the highest ratio of organic material (Fig. 2e). The pattern observed suggests that employing a higher concentration of (DEPS) led to an increased extent of sulfonamide function formation, and conversely, a lower concentration yielded a diminished effect. Finally, all these illustrated IR values are considered high evidence for the chemical reactions depicted in Scheme 1.

**3.3.3. Surface morphology of the modified polymer.** Scanning electron microscopy (SEM), a prevalent technique for surface imaging, was used to analyze the morphological characteristics of chitosan (CH) and modified chitosan-sulfonamide CHDEPS. The SEM study was performed at a liquid nitrogen temperature, with magnifications of 1000× and 2000×. Additionally, Fig. 3 illustrates the structural morphological differences between pristine chitosan and its sulfonamide derivatives. Images of native chitosan's surface showed a consistent, dense structure that was smooth and uniform in size. So, the intermolecular hydrogen bonding between nearby chitosan monomer units probably caused the observed feature.[50] Furthermore, the chitosan polymer comprises amino ($-NH_2$) groups that alternate or are on different ends of the polymer chain, indicating that it is syndiotactic and stereospecific (Fig. 3a and b). The polymer's flat, stiff, and closely packed surface is consistent with its crystalline nature. Generally, in a syndiotactic polymer, the main chain has two chiral or prochiral atoms with distinct stereochemistry inside its configurational basis unit. This configuration contributes to the structural characteristics and behavior of the polymer by ensuring that the atoms or groups involved are in a specified spatial orientation.[51]

Nonetheless, the chemical modification of CH led to significant changes in the surface morphology, resulting in a porous, crystalline and rigid texture. The altered chitosan surface exhibited new reactive sites or bonding, validating the robust interaction between phthalazine sulfonyl chloride (DEPS) and chitosan, leading to the establishment of a sulfonamide within the polymeric chain. Combining an organic sulfonamide function ($-SO_2NH$) into chemically modified chitosan resulted in a structure characterized by irregular sizing, distinct layering, enhanced porosity, and a lower rough texture, which is enhanced toward a crystalline shape. In addition, the crystalline characteristics of chitosan were altered following its association with sulfonamide derivatives of natural polymers, as

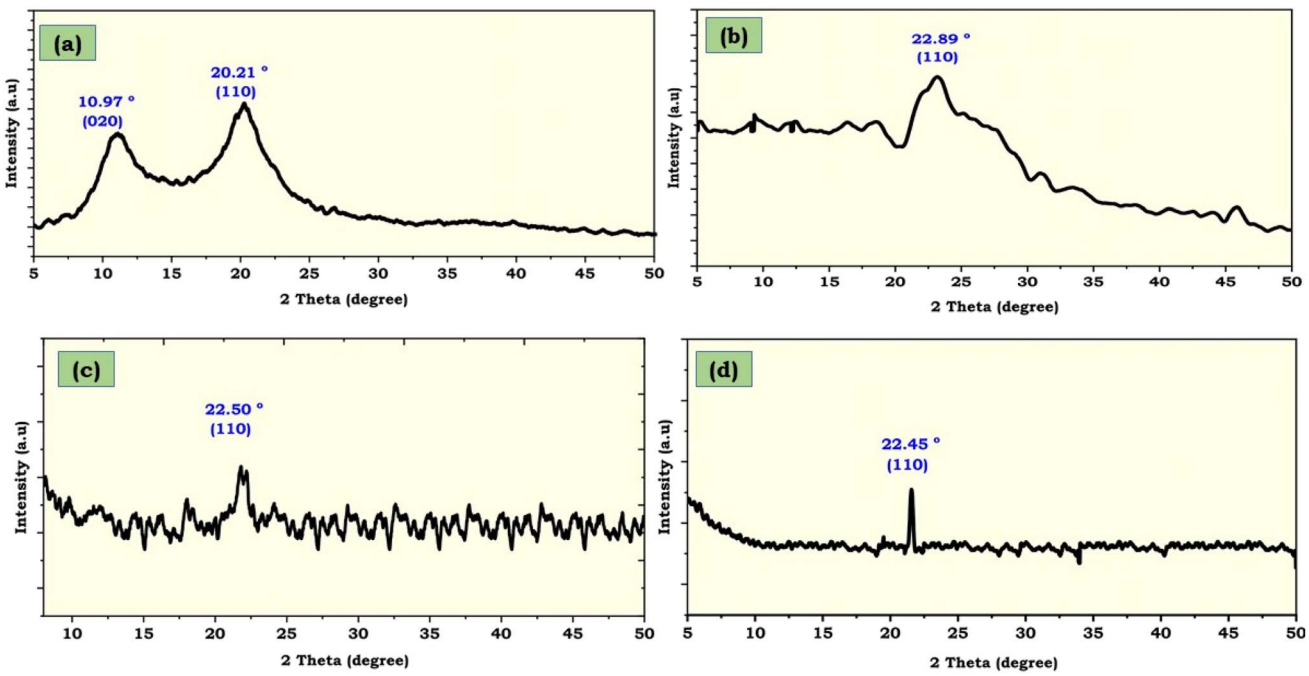


Fig. 4 XRD pattern charts of (a) CH, (b) CH-DEPS1, (c) CH-DEPS2, and (d) CH-DEPS3.

substantiated by thorough XRD analyses. The new synthesized materials exhibited distinct size and characteristics compared to CH, indicating a strong sulfonamide bond formation. Different chitosan–DEPS ratios were used to induce varying degrees of sulfonamide formation, thereby influencing morphology. Using a high ratio of CHDEPS3 in sample DEPS results in a smoother surface and more crystalline-like rods than the other ratio, attributed to the formation of a significant amount of sulfonamide groups. The substantial quantity of DEPS reacts with chitosan, filling pores and yielding a crystalline morphology (Fig. 3g and h). Additionally, the XRD analysis confirmed the crystallinity of the higher ratio sample, CHDEPS3, which is consistent with its features observed in the SEM images. Conversely, CHDEPS1 and CHDEPS2 materials exhibit smoother, porous structures and lower crystallinity than those of the CH-DEPS3 sample. It was noted that the highly smoother, porous structures and higher crystallinity of the prepared materials can be ordered by increasing the amount of organic DEPS material as follows: CH-DEPS3 > CH-DEPS2 > CH-DEPS1. Finally, these features render the materials exceptionally suitable for many industrial applications, particularly in water treatment and corrosion inhibition.[52]

**3.3.4. XRD analysis.** Fig. 4 illustrates the X-ray diffraction pattern of chitosan CH and chitosan-DEPS sulfonamide derivatives. The native chitosan exhibits two crystalline reflections at $2\theta$ values of 10.97° and 20.21°, which have been indexed as the (020) and (110) crystallographic planes, respectively (Fig. 4a). The observed diffraction peaks at $2\theta$ angles of 10.97° and 20.21° indicate the presence of partial crystallinity within the chitosan polymer. Moreover, the XRD spectrum of the unmodified chitosan CH exhibited hydrated polymorphism, characterized by the 020 reflection at 10.97° ($d$-spacing of 7.54 Å), indicative of the "tendon" form.[53] Alteration of chitosan *via* the formation of modified chitosan sulfonamide CHDEPS induced a significant alteration in XRD patterns, as the 020-plane vanished in all modified materials, indicating that the modification procedure led to changes in the enhanced crystallinity and crystal structure of chitosan (Fig. 4b–d).[54] Additionally, in all the modified materials CHDEPS1, CHDEPS2, and CHDEPS3, there is a noticeable shift of $2\theta$ from 20° to higher values, 22.89°, 22.5°, and 22.45°, respectively, and a reduction in the strength of the peak associated with the plane 110. The modified chitosan sulfonamide materials showed a decrease in the $d$-spacing value of 110 reflections compared to unmodified chitosan, as follows: CH-DEPS3 < CH-DEPS2 < CH-DEPS1 < CH. The reduction in $d$-spacing indicates a decrease in the distance between the crystal lattice planes within the material, signifying lattice contraction and phase transformations to structures characterized by smaller unit molecules. Moreover, the crystalline index provides a fundamental attribute that delineates the structural properties of chitosan, which can be determined using the area under the peak of the XRD graph. The crystallinity index of the native CH recorded 64%, while the modified chitosan CH-DEPS1, CH-DEPS2, and CH-DEPS3 showed an increase to 65%, 68.34%, and

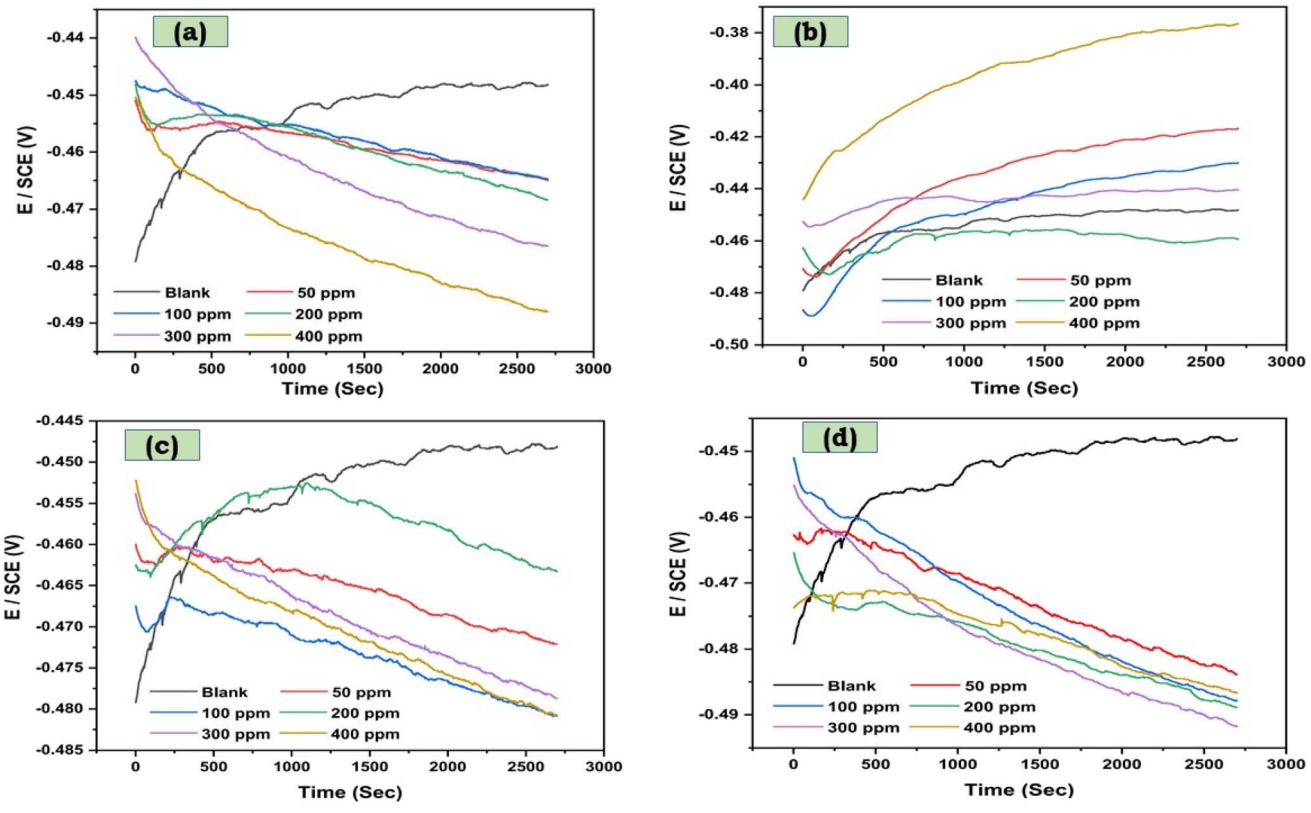


Fig. 5 Electrochemical impedance, including Nyquist plots of carbon steel in 1.0 M HCl with various doses of: (a) CH, (b) CHDEPS1, (c) CHDEPS, (d) CHDEPS3.

79.80%, respectively. By screening the charts (Fig. 4b–d), increasing the quantity of organic material DEPS in the reaction with chitosan to produce the modified chitosan sulfonamide creates a distinct, significant change in the crystal structure of chitosan. The high concentration of organic material in the CHDEPS3 sample provided the highest crystalline structure, as displayed in Fig. 4d. This change results in a substantial increase in the crystalline index of the modified chitosan, indicating a shift toward an ordered structure and potentially impacting its physical properties compared to pristine chitosan. Additionally, the increased crystallinity of modified materials can be attributed to the presence of many heteroatoms (O, N, and S) in the organic materials DEPS, which play a crucial role in hydrogen bonding formation. The increase in crystallinity of the structure is considered a promising value to enhance target applications, especially in corrosion inhibition.

### 3.4. Electrochemical investigations

**3.4.1. Open circuit potential measurements (OCP).** The Open circuit potential (OCP) technique, a readily measurable electrochemical parameter, provides preliminary information on the nature of current processes occurring at the metal/electrolyte interface, such as corrosion and passivation. Fig. 5 illustrates the evolution of the OCP for the low carbon steel electrode immersed in a 1.0 M HCl solution. This data shows the effect of adding different concentrations of chitosan and their modified samples compared to the uninhibited blank solution.

The analysis of the Open circuit potential (OCP) evolution reveals two key features regarding electrode behavior and the inhibitor mechanism. First, for the uninhibited (blank) and, the electrode potential initially shifts towards more positive values upon immersion. This immediate positive decay suggests the rapid dissolution of the pre-immersion air-formed oxide film before the system reaches its steady-state.[55] This behavior signifies that the anodic processes (film dissolution) are less

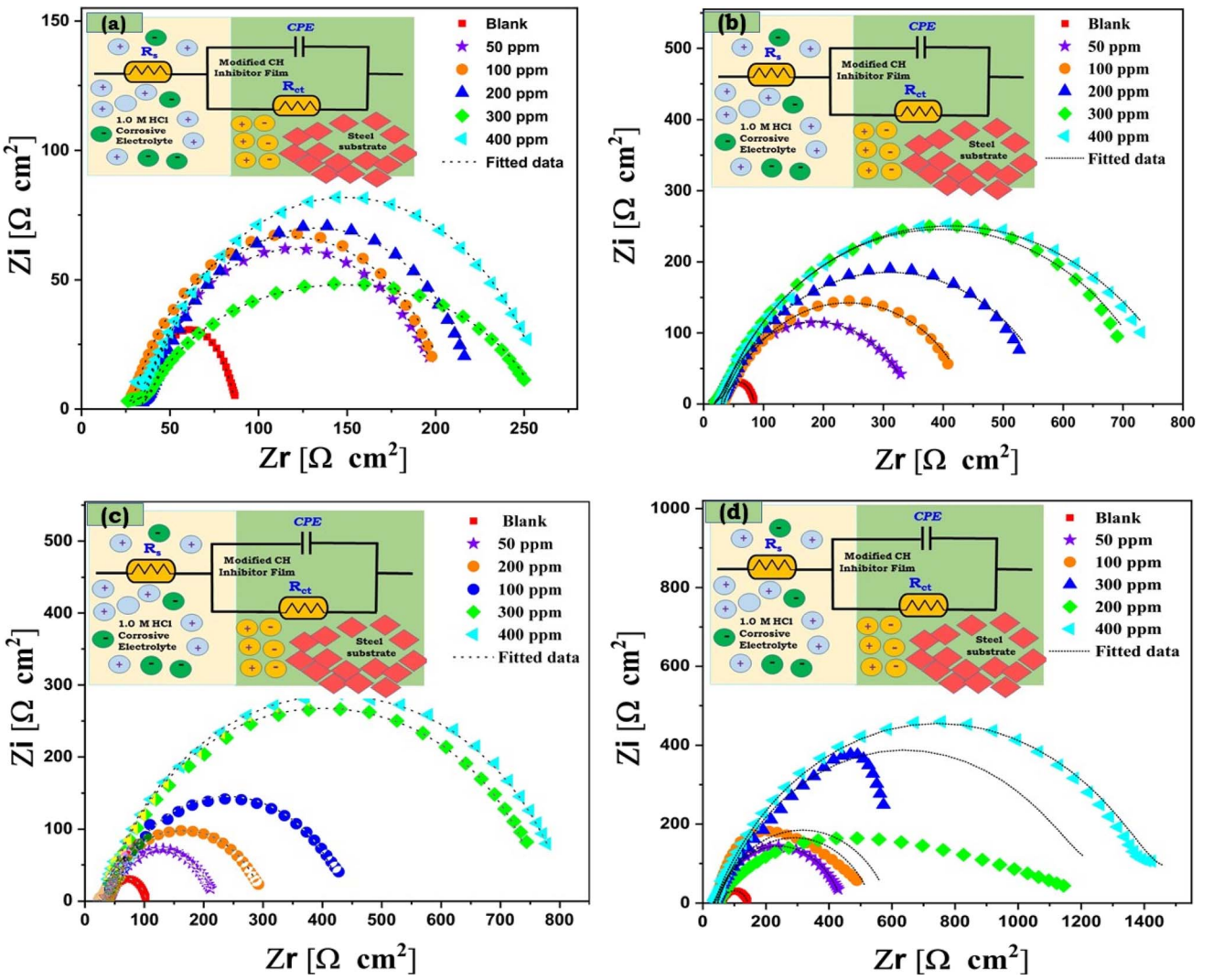


Fig. 6 Electrochemical impedance, including Nyquist plots of carbon steel in 1.0 M HCl with various doses of: (a) CH, (b) CHDEPS1, (c) CHDEPS, (d) CHDEPS3.

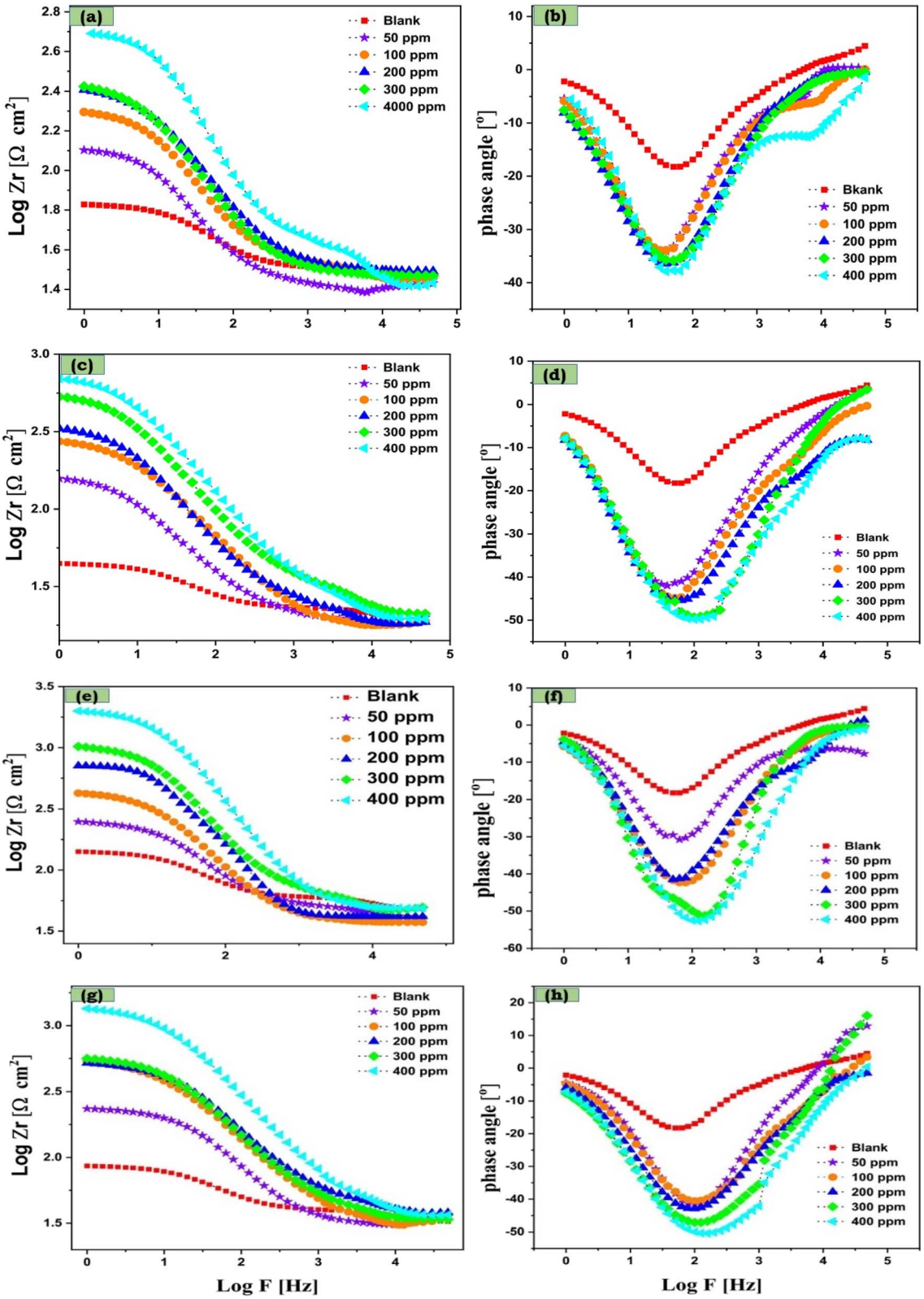


Fig. 7 Electrochemical impedance including Bode plots and Phase angle of carbon steel in 1.0 M HCl with various doses of: (a and b) CH, (c and d) CHDEPS1, (e and f) CHDEPS2, (g and h) CHDEPS3.

predominant than the cathodic processes (film formation) during the initial period, meaning the rate of oxide dissolution exceeds its rate of reformation. Next, in the presence of the inhibitors, the electrode potential stabilizes at a more negative OCP compared to the blank solution indicating the inhibitors change the kinetics of steel corrosion and inhibit oxide film

formation due to adsorption of inhibitors molecules on the steel surface. This significant positive shift suggests that the primary mechanism of corrosion protection is the adsorption of the inhibitor's active constituents onto the metal surface.[56] The resulting protective layer effectively reduces the metal's tendency to dissolve, leading to the observed shift toward lower potential. Furthermore, the CH-DEPS3 inhibitor recorded a higher protective layer, and can be ordered as follows: DEPS3 > DEPS2 > DEPS1 > CH.

**3.4.2. Electrochemical impedance spectroscopy measurements.** EIS experiments were conducted to investigate and compare the inhibition behavior of the native chitosan CH and its modified sulfonamide CHDEPS. Fig. 6 and 7 illustrates the Nyquist plot and Bode graphs of the low carbon steel sample in 1.0 M HCl corrosive solution, in the absence and presence of chitosan CH and different concentrations of modified chitosan sulfonamide CH-DEPS1, CHDEPS2, and CHDEPS3 inhibitors. The impedance in the blank solution is exceedingly low, indicating that the carbon steel endured significant corrosion in the test medium. By adding organic inhibitors, either native or modified, to the corrosive solution, a notable expansion of the capacitive semicircle is observed in the Nyquist plots, as illustrated in Fig. 6(a–d). The expansion of the capacitive semicircle correlates with the rise in the concentration of the organic inhibitors, with the highest capacitive semicircle observed at the 400 ppm solution concentration. However, when the concentration of some inhibitors reaches 400 ppm, the width of the capacitive semicircle marginally decreases. The result might be that this concentration is near or equal to the critical micelle concentration.[57] Furthermore, the capacitive semicircle of the modified chitosan sulfonamide CH-DEPS is larger than that of the native chitosan CH at the same concentration, suggesting that the modified chitosan sulfonamide CH-DEPS enhanced the inhibition efficiency of chitosan, and has a higher inhibition efficiency than native chitosan. Additionally, the capacitive semicircle of the modified chitosan sulfonamide CH-DEPS increases with the degree of sulfonamide group incorporation into chitosan, achieved by introducing the phthalazine nucleus, increasing the inhibition efficiency percentage. As a result, CH-DEPS3 has a higher capacitive semicircle and inhibition efficiency percentage, and can be ordered as follows: DEPS3 > DEPS2 > DEPS1 > CH.

To match the EIS of carbon steel samples, we used the equivalent circuit model included with Nyquist plots in Fig. 6(a–d). The fitted impedance parameters consist of the resistance of the testing medium ($R_s$), the resistance associated with the charge transfer process ($R_{ct}$), the constant phase elements of double-layer capacitance ($Q_{dl}$), and the chi-square ($\chi^2$), which is utilized to assess the precision of the fitted data, with a lower value indicating a higher quality of fitting, were depicted in Table 2. Additionally, the inhibition efficiency percentage ($\eta_{EIS}$%) was calculated using eqn (3) and is listed in Table 2. The equivalent circuit composed of solution resistance ($R_s$), connected to two parallel components, a constant phase element (CPE) and a charge transfer resistance ($R_{ct}$), which is utilized to assess the precision of the fitted data, with a lower value indicating a higher quality of fitting, is depicted in Table 2. CPE was used to deal with the non-ideal capacitance response. The fitted data show that the chi-square ($\chi^2$) values are around $10^{-6}$. A lower value of $\chi^2$ confirms the better agreement between the fitted data and the experimental results. The impedance of constant phase element ($Z_{CPE}$) and the double layer capacitance ($C_{dl}$) are calculated using the following equations:

$$Z_{CPE} = [Y_0(j\omega)^n]^{-1} \quad (7)$$

$$C_{dl} = (Y_0 R_{ct}{}^{1-n})^{1/n} \quad (8)$$

Table 2 EIS parameters for low carbon steel in 1.0 M HCl solution containing various doses of the synthesized inhibitors at 298 K

| Inhibitor | Conc. (ppm) | $R_s(R_u)$ ($\Omega$ cm$^2$) | $R_{ct}(R_p)$ ($\Omega$ cm$^2$) | $Y_0$ ($\mu\Omega^{-1}$ s$^n$ cm$^{-2}$) | $N$ | $C_{dl}$ ($\mu$F cm$^{-2}$) | $\theta$ | Chi-square ($\chi^2$) | $\eta_{EIS}$ (%) |
|---|---|---|---|---|---|---|---|---|---|
| Blank | 0.0 | 58.24 | 85.18 | 198 | 0.78 | 66.90 | — | $214 \times 10^{-6}$ | — |
| CH | 50 | 17.58 | 152.8 | 408 | 0.69 | 117.27 | 0.44 | $822 \times 10^{-6}$ | 44.25 |
| | 100 | 29.53 | 208.7 | 289.5 | 0.72 | 97.20 | 0.59 | $38.9 \times 10^{-6}$ | 59.19 |
| | 200 | 25.02 | 214.3 | 237.6 | 0.74 | 83.46 | 0.60 | $109 \times 10^{-6}$ | 60.25 |
| | 300 | 35.8 | 221.95 | 190.7 | 0.78 | 78.16 | 0.61 | $342 \times 10^{-6}$ | 61.62 |
| | 400 | 30.9 | 262.6 | 164 | 0.73 | 51.25 | 0.67 | $492 \times 10^{-6}$ | 67.56 |
| CHDEPS1 | 50 | 18.8 | 367.8 | 104 | 0.72 | 29.00 | 0.77 | $682 \times 10^{-6}$ | 76.84 |
| | 100 | 33.21 | 417.4 | 99 | 0.76 | 36.20 | 0.80 | $136 \times 10^{-6}$ | 79.59 |
| | 200 | 21.9 | 628.3 | 86 | 0.77 | 35.93 | 0.86 | $401 \times 10^{-6}$ | 86.44 |
| | 300 | 28.7 | 737.7 | 74 | 0.77 | 31.00 | 0.88 | $263 \times 10^{-6}$ | 88.45 |
| | 400 | 19.51 | 790 | 54 | 0.7 | 14.2 | 0.9 | $473 \times 10^{-6}$ | 89.69 |
| CHDEPS2 | 50 | 43.86 | 228.1 | 162 | 0.72 | 38.60 | 0.63 | $180 \times 10^{-6}$ | 63.00 |
| | 100 | 24.59 | 297.8 | 137 | 0.72 | 40.85 | 0.73 | $665 \times 10^{-6}$ | 73.40 |
| | 200 | 37.06 | 410 | 58 | 0.78 | 7.63 | 0.79 | $285 \times 10^{-6}$ | 79.22 |
| | 300 | 34.87 | 743.2 | 36.7 | 0.81 | 15.51 | 0.89 | $515 \times 10^{-6}$ | 89.34 |
| | 400 | 29.95 | 835.9 | 31.15 | 0.80 | 12.79 | 0.90 | $385 \times 10^{-6}$ | 90.06 |
| CHDEPS3 | 50 | 44.85 | 400.4 | 47.4 | 0.8 | 17.59 | 0.79 | $241 \times 10^{-6}$ | 78.73 |
| | 100 | 38.74 | 537.3 | 66.18 | 0.74 | 20.49 | 0.84 | $432 \times 10^{-6}$ | 84.15 |
| | 200 | 35.03 | 713.7 | 49.5 | 0.73 | 14.38 | 0.88 | $536 \times 10^{-6}$ | 88.07 |
| | 300 | 36.24 | 1467 | 28.6 | 0.75 | 9.94 | 0.94 | $789 \times 10^{-6}$ | 94.19 |
| | 400 | 44.94 | 1526 | 23.3 | 0.73 | 6.26 | 0.94 | $633 \times 10^{-6}$ | 94.42 |

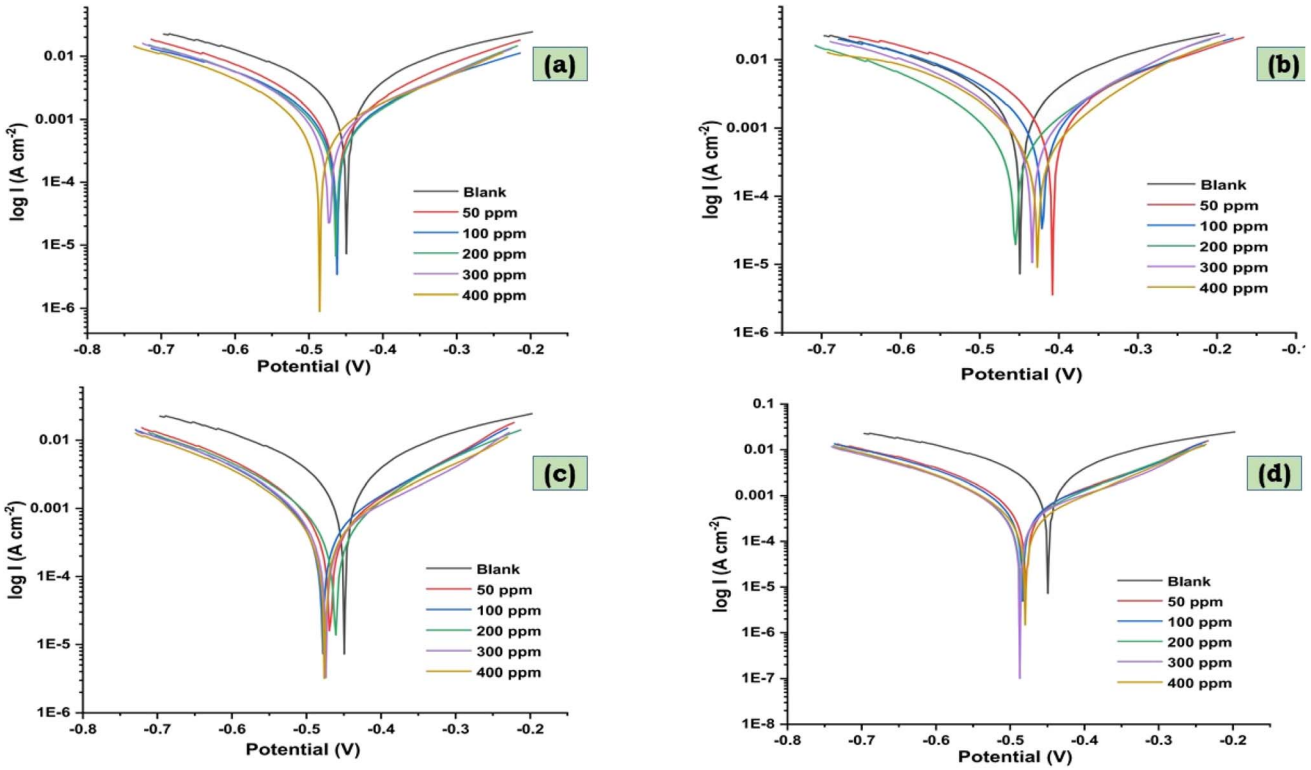


Fig. 8 The potentiodynamic polarization measurements of carbon steel in 1.0 M HCl with various doses of: (a) CH, (b) CHDEPS1, (c) CHDEPS2, (d) CHDEPS3.

where $Y_0$ = magnitude of the CPE, $n$ = CPE exponent, $\omega$ = angular frequency and $j = (-1)^{1/2}$.

Table 2 illustrates that the $R_{ct}$ values increase with higher concentrations of chitosan CH and modified chitosan sulfonamide CH-DEPS1, CH-DEPS2, and CH-DEPS3 within the 50–400 ppm range. Additionally, the modified chitosan sulfonamide CHDEPS exhibited the highest $R_{ct}$ values compared to those in the native chitosan CH, and the CHDEPS3 sample achieved the highest $R_{ct}$ value. The value of $R_{ct}$ is 85.18 Ω cm$^2$ in the blank solution, which does not include the organic inhibitors. However, the $R_{ct}$ values reach 262.60 Ω cm$^2$ with the addition of 400 ppm of native chitosan CH. While investigating the modified chitosan sulfonamides CHDEPS1, CHDEPS2, and CHDEPS3, the $R_{ct}$ values were found to be 790.10 Ω cm$^2$, 835.90 Ω cm$^2$, and 1526 Ω cm$^2$, respectively. In alignment with this, the inhibition efficiencies of chitosan were recorded at 67.56%, while those of modified chitosan CHDEPS1, CHDEPS2, and CHDEPS3 were 89.69%, 90.06%, and 94.42%, respectively. This demonstrates that the modified chitosan sulfonamide displays remarkable inhibition capabilities even at relatively low concentrations (400 ppm). In particular, the CHDEPS3 had a stronger inhibitory impact than CHDEPS1 or CHDEPS2, suggesting that increasing the modification of chitosan into modified chitosan sulfonamide greatly enhanced the corrosion inhibition percentage. Furthermore, the depression in $C_{dl}$ values may be attributed to a decrease in the local dielectric constant and/or an increase in the thickness of the electrical double layer. Additionally, as illustrated in the Bode phase and Bode angle plots, Fig. 7(a–h), the maximum phase angle increases and shifts to the high-frequency region with rising dose concentration of the inhibitors, indicating a higher capacitive response of the adsorbed inhibitor layer.[58]

**3.4.3. Potentiodynamic polarization measurements.** Potentiodynamic polarization measurements at room temperature were used to assess the kinetics of cathodic and anodic reactions at a low-carbon steel electrode in a 1.0 M HCl solution, with and without varying CHDEPS concentrations. Fig. 8 illustrates the polarization curves of CS in both chitosan derivative-free and containing chitosan derivatives. In addition, the related electrochemical parameters such as corrosion current density ($I_{corr}$), corrosion rate ($K_{corr}$), corrosion potential ($E_{corr}$), corrosion inhibition efficiency ($\eta_{pol}$%), and cathodic Tafel slope ($\beta_a$, $\beta_c$) are calculated and listed in Table 3. In comparison to the untreated corrosive solution (Blank), the polarization curves in the treated solution shift to the lower current density zone, indicating that both anodic and cathodic densities decrease when CH or CHDEPS is added. In the meantime, introducing CH or CHDEPS results in a slight shift of the corrosion potential ($E_{corr}$) towards either a negative or positive direction, indicating that CH and CHDEPS function as mixed-type corrosion inhibitors.[59] Nevertheless, according to the previously reported article, the chitosan CH is not sufficiently excellent as an organic inhibitor. We investigated the polarization measurements for the CH and the different concentrations of modified chitosan CHDEPS1, CHDEPS2, and CHDEPS3 to enhance the corrosion inhibition of chitosan. It was found that the $I_{corr}$ in the case of the blank solution, which recorded 454 μA cm$^{-2}$, indicates that the metal surface is exposed to a highly corrosive process. By

 

Table 3 Potentiodynamic polarization associated parameters for low carbon steel in 1.0 M HCl solution containing various doses of the synthesized inhibitors at 298 K

| Inhibitor | Conc. (ppm) | $I_{corr}$ (μA cm$^{-2}$) | $E_{corr}$ (mV *vs.* SCE) | $\beta_a$ (mV dec$^{-1}$) | $\beta_c$ (mV dec$^{-1}$) | $K$ (mm y$^{-1}$) | $\eta_{pol}$% |
|---|---|---|---|---|---|---|---|
| Blank | 0.0 | 2661 | −449 | 140 | 155 | 30.92 | 0.00 |
| CH | 50 | 1070 | −462 | 262 | 181.1 | 12.43 | 59.79 |
| | 100 | 1010 | −463 | 195 | 158 | 11.73 | 62.04 |
| | 200 | 930 | −464 | 228 | 159 | 10.80 | 65.05 |
| | 300 | 813 | −473 | 251 | 162 | 9.44 | 69.45 |
| | 400 | 720 | −485 | 330 | 173 | 8.36 | 72.94 |
| CHDEPS1 | 50 | 921 | −408 | 157.6 | 128 | 10.70 | 65.39 |
| | 100 | 686 | −421 | 197.6 | 177.7 | 7.97 | 74.22 |
| | 200 | 543 | −455 | 159 | 141 | 6.31 | 79.59 |
| | 300 | 367 | −434 | 153.8 | 141.6 | 4.26 | 86.21 |
| | 400 | 258 | −427 | 141 | 125 | 3.00 | 90.30 |
| CHDEPS2 | 50 | 507 | −469 | 184.6 | 137.8 | 5.89 | 80.95 |
| | 100 | 440 | −478 | 213 | 146 | 5.11 | 83.46 |
| | 200 | 393 | −474 | 312 | 156.7 | 4.57 | 85.23 |
| | 300 | 195 | −461 | 170.4 | 151 | 2.27 | 92.67 |
| | 400 | 162 | −476 | 193.5 | 135.9 | 1.88 | 93.91 |
| CHDEPS3 | 50 | 5.61 | −479 | 209 | 135 | 5.61 | 81.85 |
| | 100 | 4.79 | −483 | 293 | 160 | 4.79 | 84.52 |
| | 200 | 3.92 | −487 | 278 | 150 | 3.92 | 87.34 |
| | 300 | 2.25 | −486 | 182 | 134.5 | 2.25 | 92.71 |
| | 400 | 1.43 | −480 | 191 | 132.5 | 1.43 | 95.38 |

adding the chitosan CH inhibitor, the $I_{corr}$ decreases to 720 μA cm$^{-2}$. At the same time, the modified chitosan sulfonamide inhibitors, CHDEPS1, CHDEPS2, and CHDEPS3, recorded lowest $I_{corr}$ values of 258, 162, and 1.43 μA cm$^{-2}$, respectively, at 400 ppm. Additionally, it represents enhanced inhibition efficiencies, increasing from 72.94% for CH to 90.30%, 93.91%, and 95.38% for CHDEPS1, CHDEPS2, and CHDEPS3, respectively (Table 3). For explanation, the addition of modified chitosan inhibitors CHDEPS significantly reduces $I_{corr}$, indicating that these three modified chitosan sulfonamides exhibit excellent inhibitory performance. As observed in Fig. 6 and 7, the $I_{corr}$ was decreased by increasing the concentration of phthalazine material DEPS to the chitosan structure for chemical synthesis of CHDEPS, meaning that the $I_{corr}$ was ordered as follows: CHDEPS3 < CHDEPS2 < CHDEPS1, indicating the superior inhibitory efficacy of CHDEPS3. Consequently, CHDEPS3 demonstrates greater efficacy in inhibiting the corrosion process of CS than the other two concentrations. The presence of chitosan in the solution reduces the cathodic current density, while both the anodic and cathodic current densities decrease with the addition of CHDEPS to the solution. Additionally, the anodic and cathodic current densities were significantly reduced in the case of the CHDEPS3 solution. It can be attributed to the two carbonyl functions in the phthalazine molecule, which exhibit greater electronegativity, making it more prone to protonation and subsequently favoring adsorption in the cathodic region. Consequently, the cathodic process is inhibited due to the adsorption of inhibitors after protonation. Hence, CHDEPS may absorb both the cathodic and anodic areas, indicating that the adsorption of these inhibitors inhibits both the cathodic and anodic processes. Furthermore, $E_{corr}$ values fluctuating less than 85 mV suggest that the inhibitors should be categorized as mixed inhibitors, mostly affecting the anodic site.[60]

### 3.5. Morphological surface characterization

SEM and EDX examinations were employed to examine the surface morphology of the carbon steel samples that were immersed in a 1.0 M HCl solution for 24 h. This study was conducted on samples with and without inhibitors, namely CH, CHDEPS1, CHDEPS2, and CHDEPS3. Before exposure to a corrosive acidic solution, the surface of the carbon steel was polished, as illustrated in Fig. 9a. The extensive use of silica carbide sheets for rust treatment has left noticeable scratches on the CS surface. On the surface of the metal, it is impossible to do anything to avoid the production of these scratches, which are known as asperities. Fig. 9c presents an SEM image of the metal-carbon surface submerged in a 1.0 M hydrochloric acid solution. In the absence of an inhibitor, the metal corrosion process caused significant damage to the specimen's surface. Numerous visible holes of varying sizes and depths have formed on the carbon steel surface due to acidic corrosion. It indicates that the corrosion process has led to significant material loss.[61] The surface exhibited irregularities due to the dissolution process in the corrosive solution. Furthermore, the metal surface experienced considerable degradation due to a thick and porous layer of corrosion debris, consisting of oxide films covering the entire surface.

Furthermore, incorporating the corrosion inhibitors CH, CHDEPS1, CHDEPS2, and CHDEPS3 into the corrosive solution at a concentration of 400 ppm significantly diminished the extent of surface damage to the specimen, as demonstrated in Fig. 9e, g, i, and k. Compared to Fig. 9c, the pits and fractures were significantly less severe, as indicated by this observation.

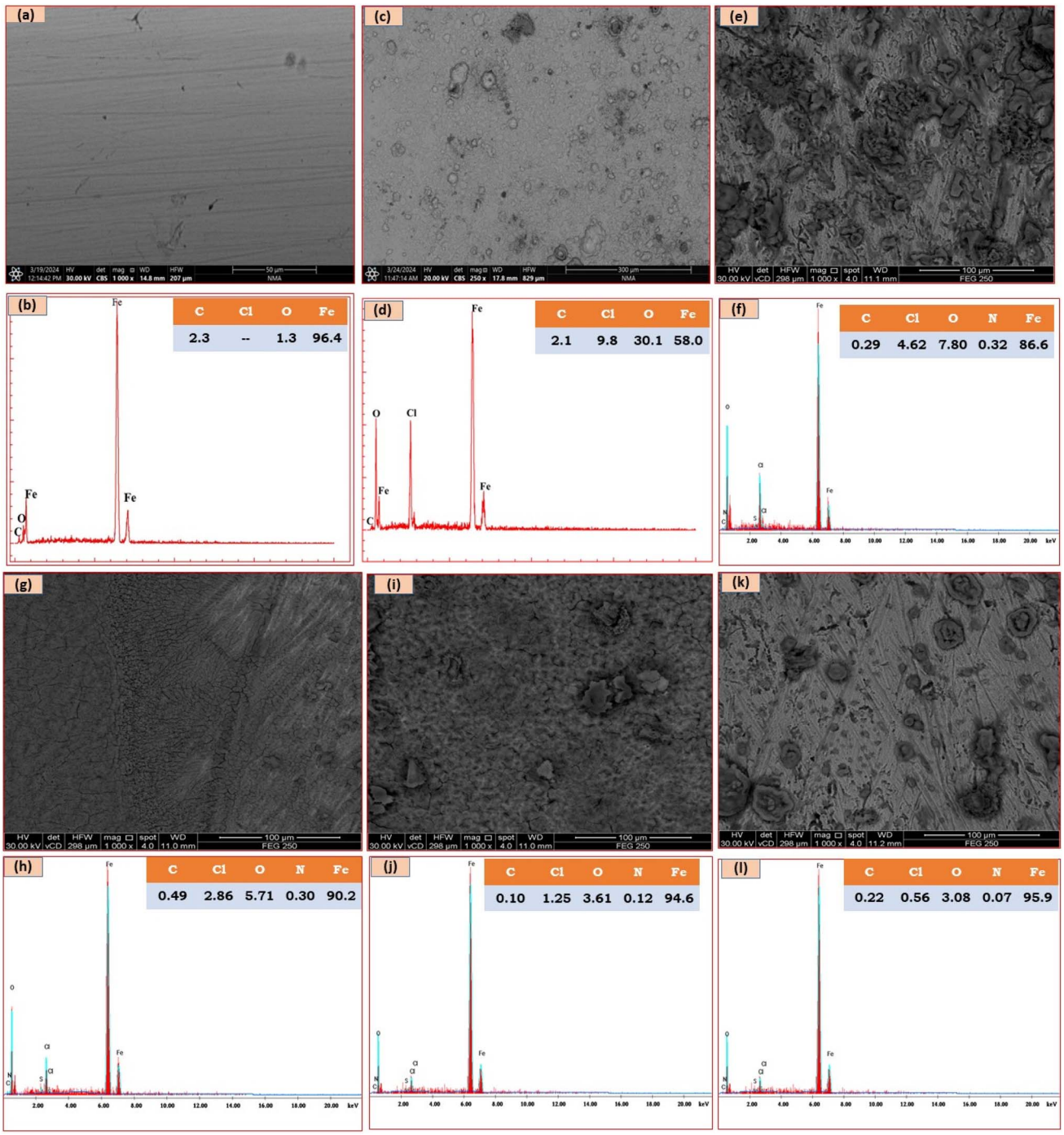


Fig. 9 SEM-EDX images of (a and b) polished carbon steel, (c and d) immersed in 1.0 M HCl for 24 h without inhibitors, (e and f) for 24 h with CH solution, (g and h) for 24 h with CH-DEPS1 solution, (i and j) for 24 h with CH-DEPS2 solution, (k and l) for 24 h with CH-DEPS3 solution.

SEM images of CS immersed in 1.0 M HCl with 400 ppm of CH show smoother surfaces and less breaking compared to previous findings. Also, the CH inhibitor appears to create a protective layer on the surface of the CS. Furthermore, the efficacy of CH, CH-DEPS1, CH-DEPS2, and CH-DEPS3 inhibitors is demonstrated by their capacity to create a protective layer that shields the metal surface from corrosive conditions in 1.0 M HCl.[62] In contrast to the CH-DEPS inhibitor, which may be uniform and adhere to the metal surface, the native Chitosan CH inhibitor seems to provide a less protective layer on the surface of the CS.

Moreover, Fig. 9b, d, f, h, j, and l present the results obtained from EDX analysis. The uppermost layer of the carbon steel exhibits the main elemental dispersion, including iron and carbon (Fig. 9b). After immersing the carbon steel sample in the corrosive solution (HCl), the EDX spectrum in Fig. 8d shows the presence of Fe and C elements, as well as a peak for the chloride ion, which is specific to the corrosive solution, besides iron

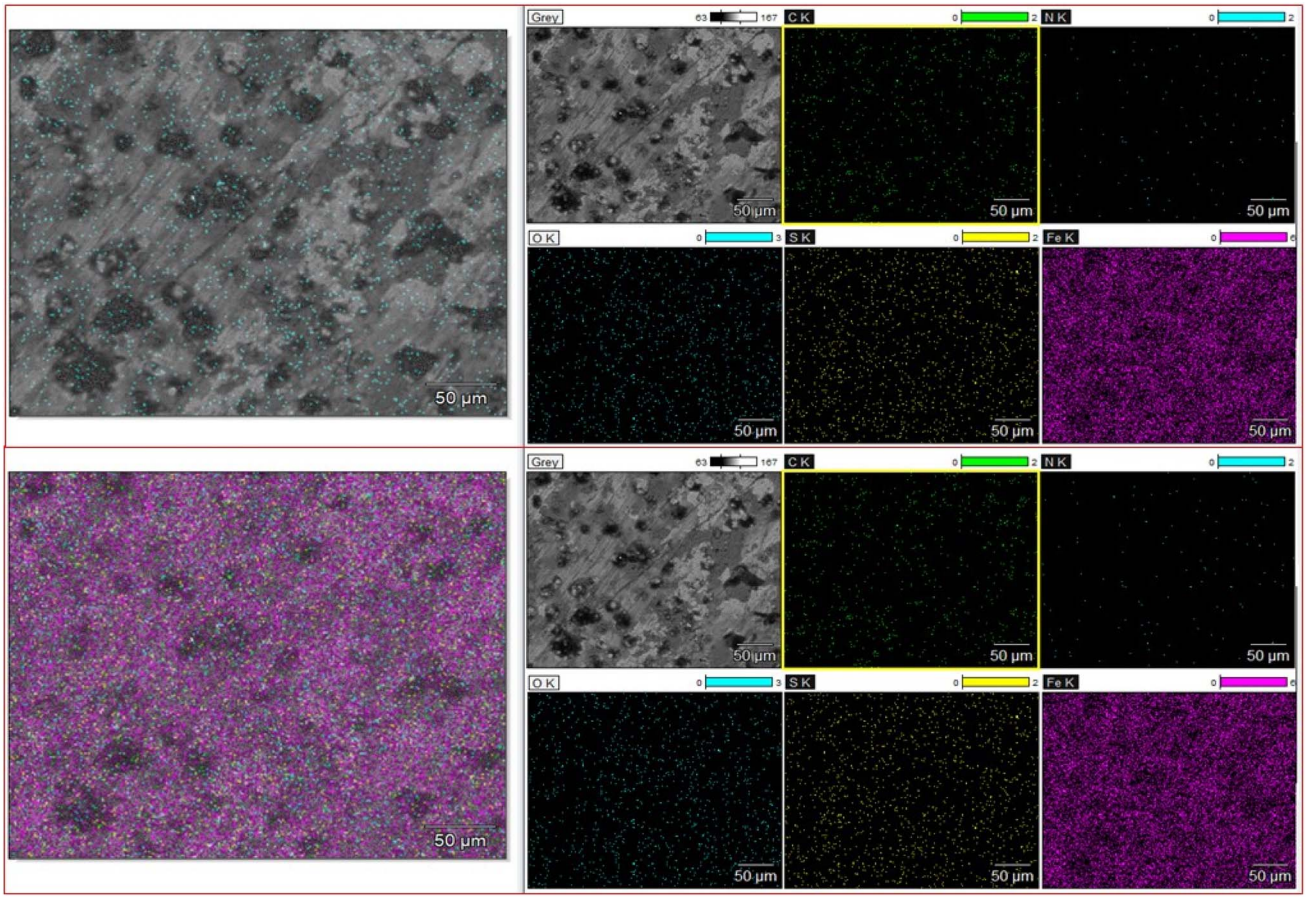


Fig. 10 SEM-EDS mapping of the main element distribution in the carbon steel sample immersed in a 400 ppm HCl-containing CHDEPS3 inhibitor for 24 h.

oxides. This indicates the accumulation of corrosion components (salts and oxides) on the steel surface. On the contrary, adding the target inhibitors CH, CHDEPS1, CHDEPS2, and CHDEPS3 resulted in a low nitrogen content by weight and reduced the peaks associated with corrosion salts and oxides. The chitosan inhibitor CH displayed the lowest intensity peak for iron (86.6%) and a peak for the chloride ion (Fig. 8f). In contrast, the modified chitosan inhibitors CHDEPS1, CHDEPS2, and CHDEPS3 showed the highest intensity peak of iron compared to CH, with CH-DEPS3 exhibiting the most pronounced intensity iron peak (Fig. 9h, j, and l). For more details, the CHDEPS1 inhibitor contained approximately 90.2% iron, whereas the CH-DEPS2 and CH-DEPS3 inhibitors contained approximately 94.6% and 95.9% iron, respectively. Thus, the findings unambiguously confirm the presence of protective layers on the CS surface. The findings indicated that the CHDEPS3 inhibitor forms a more effective protective coating on the steel surface compared to other inhibitors, ranked as follows: CHDEPS3 > CHDEPS2 > CHDEPS1> CH.

Consequently, SEM-EDS mapping of the best protective sample, CH-DEPS3, was conducted to reveal the primary composition and the underlying reasons for the formation of these precipitates. Fig. 10 illustrates that the precipitates primarily consist of iron, which is the main component of the samples, and have a low carbon content. Additionally, these precipitates are composed not only of iron but also of N, O, and S elements, which are the chemical components of the inhibitor CHDEPS3. It indicates that the organic components of the CHDEPS3 inhibitor were uniformly dispersed on the surface of the sample through its dissolution in the corrosive medium (HCl solution). After that, this organic component absorbs and creates a protective layer on the steel.[63] This film obstructs the active sites and diminishes the anodic dissolution of the steel sample. It appeared that this layer was sufficient to cover the metal surface, which could provide a highly corrosion-inhibiting characteristic.

### 3.6. AFM analysis

SEM micrographs do not provide quantitative information on the roughness of carbon steel in the absence or presence of inhibitors. As a result, AFM was employed further to investigate the surface morphology of the CS surface. Fig. 11a–d depicts the 3D micrograph of CS under different conditions. The average roughness value of the polished carbon steel sample (Fig. 11a) was 9.33 nm, while that of the sample immersed in 1.0 M HCl solution without an inhibitor was increased to 852 nm, as viewed in Fig. 11b. Due to the acidic damage environment, a higher surface roughness of CS exposed to blank solution displays a bumpy structure with many ups and downs. Nevertheless, at the optimal concentration (400 ppm) of the CHDEPS3 inhibitor, the average roughness value

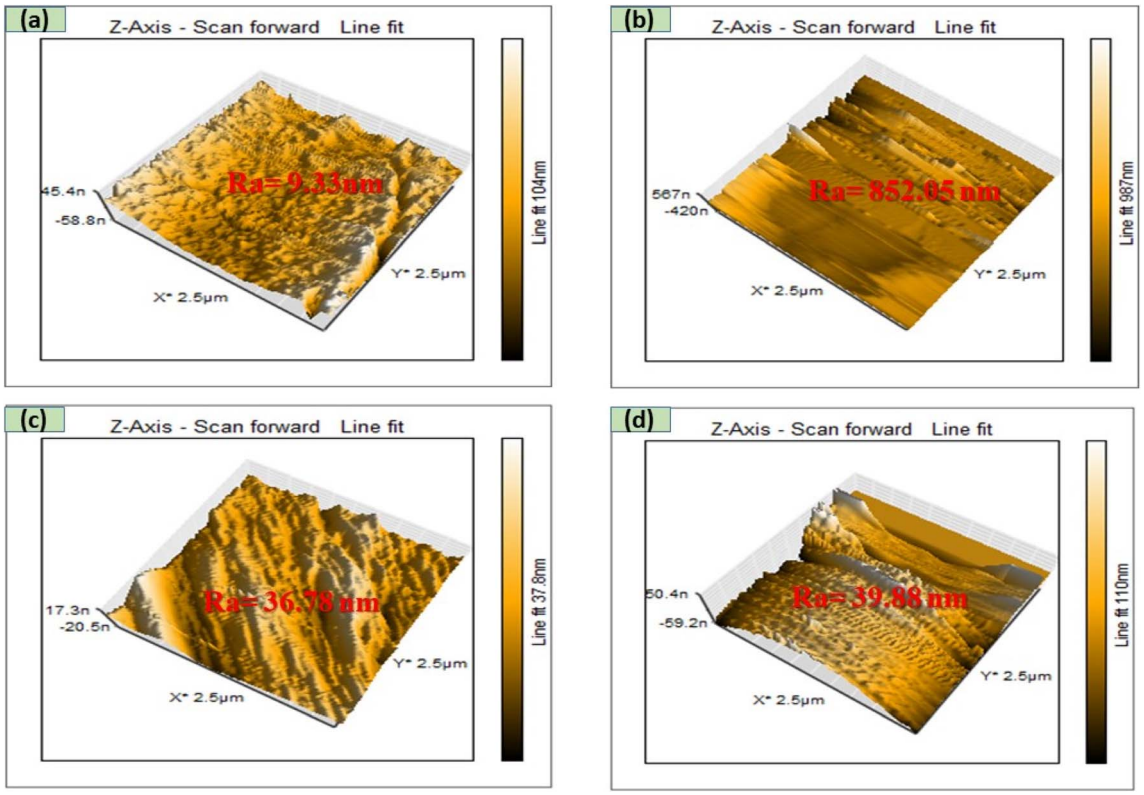


Fig. 11 AFM micrographs of (a) polished mild steel surface, (b) mild steel in 1.0 M HCl, and (c and d) mild steel in 1.0 M HCl in the presence of 400 ppm of CHDEPS3 inhibitor.

decreased to 36.78 and 39.88 nm, respectively, as viewed in Fig. 11c and d. It can be noted that while adding an inhibitor to an acid solution, the surface shape of carbon steel altered owing to the creation of an adsorbed protective layer.[64]

### 3.7. Weight loss measurements

**3.7.1. Effect of concentration.** The efficacy of corrosion inhibition by the newly synthesized inhibitors was assessed using the weight loss technique, a straightforward and economically viable method. This strategy leads to a certain amount of weight reduction and inhibition efficiency. Fig. 12a and b depicts the relation between concentration of inhibitors and corrosion rate or inhibition efficiency during immersion process on carbon steel in 1.0 M HCl medium at 298 K in the absence and presence of various inhibitor doses in ppm (50, 100, 200, 300 and 400 ppm). As listed in Table 3, the low-carbon steel in the absence of inhibitors (blank solution) exhibits a higher corrosion rate, reaching 0.62 mg $cm^{-2}$ $h^{-1}$ at 120 hours. By adding the native chitosan CH as an organic inhibitor to the corrosive solution, the corrosion rate was reduced by 0.18 mg $cm^{-2}$ $h^{-1}$ at 400 ppm concentration, with a recorded inhibition efficiency of 71.62%. Furthermore, the modified chitosan sulfonamide inhibitors, CH-DEPS, exhibited a higher reduction in corrosion at a high concentration of 400 ppm. For

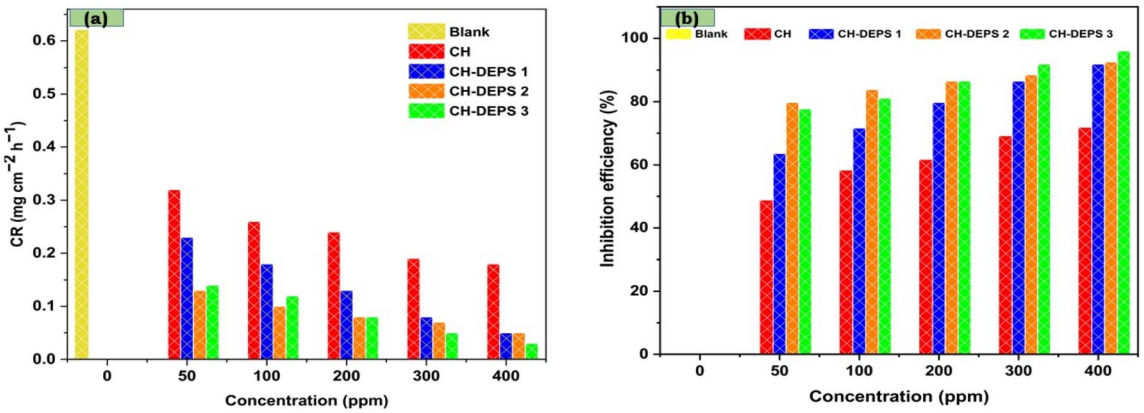


Fig. 12 The corresponding corrosion rate and inhibition efficiencies at various concentrations of inhibitors.

Table 4 Corrosion items obtained from weight loss measurements for low carbon steel in 1.0 M HCl with and without different doses of the inhibitors at 298 K and 120 h

| Inhibitor | Conc. (ppm) | Weight loss (mg) | CR (mg $cm^{-2}$ $h^{-1}$) | $\theta$ | $\eta_{WL}$ (%) |
|---|---|---|---|---|---|
| Blank | 0.0 | 74 | 0.62 | — | — |
| CH | 50 | 38 | 0.32 | 0.49 | 48.65 |
| | 100 | 31 | 0.26 | 0.58 | 58.11 |
| | 200 | 28.5 | 0.24 | 0.61 | 61.49 |
| | 300 | 23 | 0.19 | 0.69 | 68.92 |
| | 400 | 21 | 0.18 | 0.72 | 71.62 |
| CHDEPS1 | 50 | 27 | 0.23 | 0.64 | 63.51 |
| | 100 | 21 | 0.18 | 0.72 | 71.62 |
| | 200 | 15 | 0.13 | 0.80 | 79.73 |
| | 300 | 10 | 0.08 | 0.86 | 86.49 |
| | 400 | 6 | 0.05 | 0.92 | 91.89 |
| CHDEPS2 | 50 | 15 | 0.13 | 0.80 | 79.73 |
| | 100 | 12 | 0.10 | 0.84 | 83.78 |
| | 200 | 10 | 0.08 | 0.86 | 86.49 |
| | 300 | 8.5 | 0.07 | 0.89 | 88.51 |
| | 400 | 5.5 | 0.05 | 0.93 | 92.57 |
| CHDEPS3 | 50 | 16.5 | 0.14 | 0.78 | 77.70 |
| | 100 | 14 | 0.12 | 0.81 | 81.08 |
| | 200 | 10 | 0.08 | 0.86 | 86.49 |
| | 300 | 6 | 0.05 | 0.92 | 91.89 |
| | 400 | 3 | 0.03 | 0.96 | 95.95 |

more details, the three modified chitosan sulfonamides, CHDEPS1, CHDEPS2, and CHDEPS3, exhibited lower corrosion rate values of 0.05, 0.049, and 0.03 mg $cm^{-2}$ $h^{-1}$, respectively, and higher inhibition efficiencies of 91.89%, 92.57%, and 95.95%, respectively. It was noted that the modified chitosan sulfonamide exhibited the highest inhibition efficiency compared to native chitosan, and CHDEPS3 showed the best inhibition efficiency percentage (Table 4). Higher concentrations of modified chitosan sulfonamide inhibitor led to increased inhibitory efficiency and surface coverage, likely due to enhanced availability of electron donors (O, S, and N) and aromatic rings, particularly with the CHDEPS3 structure.[65] The findings confirm the hypothesis that inhibitor molecules may efficiently cover the surface of carbon steel in 1.0 M HCl medium. Furthermore, the presence of lone pairs of electrons on heteroatoms such as nitrogen, oxygen, and sulfur enhances the coordination-based adsorption of inhibitors onto the steel surface, a process documented as chemisorption. However, aromatic rings facilitate physisorption, which is a weaker physical interaction between inhibitors and the CS surface. The carbon steel surface then develops a more resilient and adhesive protective layer.[66]

**3.7.2. Effect of temperature.** The temperature is a significant factor that can alter the properties of a metal in a corrosive environment. So, this study examined the influence of temperature on metal–solution interactions, both with and without the presence of 400 ppm inhibitor such as chitosan CH and their modified sulfonamide CHDEPS, within the temperature range of 298–353 K. The relation between variable temperature and corrosion rate or inhibition efficiency is displayed in Fig. 13a and b, and the resulting data are depicted in Table 5. According to native chitosan CH as an inhibitor, the

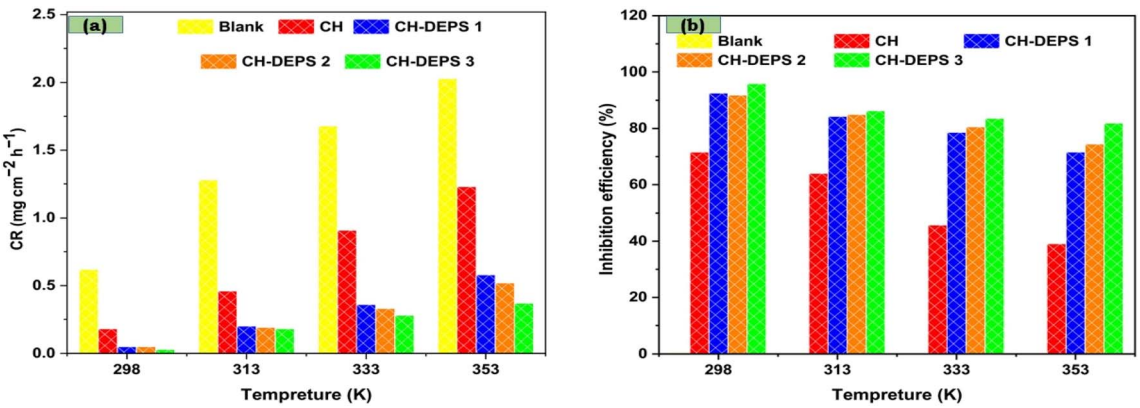


Fig. 13 The corresponding inhibition efficiencies and corrosion rate at different temperatures and higher concentrations of inhibitors (400 ppm).

Table 5 Corrosion items obtained from weight loss measurements for low carbon steel in 1.0 M HCl with 400 ppm of inhibitors at different temperatures

| Inhibitor | Temp. (K) | Weight loss (mg) | CR (mg $cm^{-2}$ $h^{-1}$) | $\theta$ | $\eta_{WL}$ (%) |
|---|---|---|---|---|---|
| Blank | 298 | T74 | 0.62 | — | — |
| | 313 | 153 | 1.28 | — | — |
| | 333 | 201 | 1.68 | — | — |
| | 353 | 243 | 2.03 | — | — |
| CH | 298 | 21 | 0.18 | 0.72 | 71.62 |
| | 313 | 55 | 0.46 | 0.64 | 64.05 |
| | 333 | 109 | 0.91 | 0.46 | 45.77 |
| | 353 | 148 | 1.23 | 0.39 | 39.09 |
| CHDEPS1 | 298 | 5.5 | 0.05 | 0.93 | 92.57 |
| | 313 | 24 | 0.20 | 0.84 | 84.31 |
| | 333 | 43 | 0.36 | 0.79 | 78.61 |
| | 353 | 69 | 0.58 | 0.72 | 71.60 |
| CHDEPS2 | 298 | 6 | 0.05 | 0.92 | 91.89 |
| | 313 | 23 | 0.19 | 0.85 | 84.97 |
| | 333 | 39 | 0.33 | 0.81 | 80.60 |
| | 353 | 62 | 0.52 | 0.74 | 74.49 |
| CHDEPS3 | 298 | 3 | 0.03 | 0.96 | 95.95 |
| | 313 | 21 | 0.18 | 0.86 | 86.27 |
| | 333 | 33 | 0.28 | 0.84 | 83.58 |
| | 353 | 44 | 0.37 | 0.82 | 81.89 |

corrosion rate is highly increased from 0.18 mg $cm^{-2}$ $h^{-1}$ at 298 K to 1.23 mg $cm^{-2}$ $h^{-1}$ at 353 K in 1.0 M HCl. Following that, the inhibition efficiency of the native Chitosan CH was changed from 71.62% at 298 K to 39.09% at 353 K in 1.0 M HCl. Conversely, the modified sulfonamides CHDEPS1, CHDEPS2, and CHDEPS3 exhibited higher stability as inhibitors with increasing temperature (Table 5). Notably, the CHDEPS3 inhibitor exhibited the best inhibitory efficiency with increasing temperature compared to CHDEPS1, CHDEPS2, and native chitosan. The CHDEPS3 inhibitor revealed a slight change in the corrosion rate from 0.03 mg $cm^{-2}$ $h^{-1}$ at 298 K to 0.37 mg $cm^{-2}$ $h^{-1}$ at 353 K in 1.0 M HCl. Additionally, the inhibition efficiency decreased slightly from 95.95% at 298 K to 81.89% at 353 K. These results indicated that the CHDEPS3 inhibitor exhibited higher inhibition efficiency and exhibited higher inhibition stability with increasing temperature. Furthermore, the study observed a decrease in inhibition efficiency with increasing temperature, attributed to the potential desorption of the inhibitor from the carbon steel surface at elevated temperatures. The efficiency of inhibition decreases because, as temperatures rise, inhibitor molecules move from the carbon steel surface to the solution, potentially exposing a large portion of the steel surface area to the corrosive medium.[67] Generally, the introduction of inhibitors leads to a notable equilibrium between adsorption and desorption processes. At higher temperatures, the adsorption intensity drops because the adsorption capacity drops, assuming physical adsorption is more effective than chemical adsorption. This occurrence may be elucidated by the presence of many aromatic rings in the structure of CHDEPS inhibitors, which facilitate physical contact between the π-bond and the metal surface. Conversely, the elevation in temperature further promotes the dissolution of carbon steel, thereby impeding the adsorption of compounds onto the metal surface.[68,69] The reduction in the protective efficacy of inhibitors with rising temperature has two implications. Initially, the balance between adsorption and desorption shifts in favor of desorption, leading to a decrease in adsorption intensity. Secondly, elevated temperatures lead to enhanced corrosion, which results in a more abrasive surface for the carbon steel.

Continuously, thermodynamic activation parameters, including apparent activation energy ($E_a^*$), enthalpy of activation ($H^*$), and entropy of activation ($S^*$), play a crucial role in determining the mechanism of corrosion inhibition. We used the Arrhenius equation to get the activation energy according to the following equation:

$$\text{Log CR} = A - \left(E_a^*/2.303RT\right) \quad (9)$$

where $A$ is the extrapolation factor, $R$ represents the universal gas constant, and $T$ signifies the absolute temperature. The lines that result from plotting log CR *vs.* $1000/T$ have a slope of $E_a^*/2.303R$ and an intercept of the constant $A$. In addition, Fig. 13 illustrates the relationship between the logarithms of corrosion rates (CR) plotted against the reciprocal of the absolute temperature ($T$) for carbon steel corrosion in 1.0 M HCl, both in the absence and presence of high concentration (400 ppm) of the inhibitors CH, and their modified sulfonamide CHDEPS. The derived values of activation energies $E_a^*$, are obtained from the slopes of the plots presented in Table 6. As a result, the activation energy value for the blank solution recorded 19.08 kJ $mol^{-1}$, while the activation energy value for the CH inhibitor slightly increased, reaching 31.96 kJ $mol^{-1}$. Furthermore, the corrosive solution included the modified chitosan inhibitors CHDEPS1, CHDEPS2, and CHDEPS3, which displayed a higher increase in the activation energy of 37.12, 40.26, and 42.44 kJ $mol^{-1}$, respectively. It was observed that the CHDEPS3 inhibitor exhibited the highest activation energy among the other modified and chitosan samples, indicating a high percentage of energy barrier formation when CHDEPS3 is present. The transition plots of $\log(R/T)$ *versus* $(1000/T)$ for carbon steel in 1.0 M HCl at various ppm concentrations of the selected inhibitors yield linear representations, as illustrated in Fig. 14, featuring a slope of $(-H^*/2.303R)$ and an intercept of $(\log R/NAh + S^*/2.303R)$. The positive and increasing values of enthalpy changed from 57.47 kJ $mol^{-1}$ for the blank solution to 105.30, 130.00, 139.77 and 150.68 kJ $mol^{-1}$ for CH, CHDEPS1, CHDEPS2, and CHDEPS3, respectively. The obtained results

Table 6 Thermodynamic parameters for 400 ppm concentration of chitosan and their modified chitosan sulfonamide onto low carbon steel in 1.0 M HCl at 298 K

| Inhibitor | $R^2$ | $E_a^*$ (kJ $mol^{-1}$) | $\Delta S$ (kJ $mol^{-1}$) | $\Delta H^*$ (kJ $mol^{-1}$) |
|---|---|---|---|---|
| Blank | 0.94 | 19.08 | −197.39 | 57.47 |
| CH | 0.95 | 31.96 | −0.53809 | 105.30 |
| CHDEPS1 | 0.96 | 37.12 | −0.5378 | 130.00 |
| CHDEPS2 | 0.94 | 40.26 | −0.53798 | 139.77 |
| CHDEPS3 | 0.95 | 42.44 | −0.53788 | 150.68 |

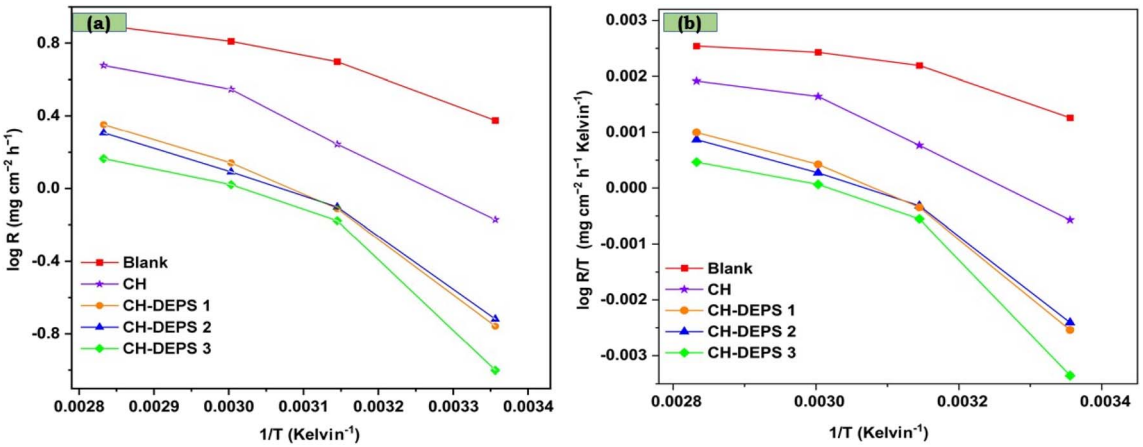


Fig. 14 Arrhenius plots (a) and transition-state plots (b) for carbon steel in 1.0 M HCl in absence and presence of 400 ppm of chitosan CH and their modified chitosan sulfonamide CH-DEPS.

demonstrate the endothermic character of the carbon steel dissolution process, suggesting sluggish dissolution in the presence of organic inhibitors, particularly in the case of the CHDEPS3 inhibitor. On the contrary, the value of entropy ($S^*$) is significantly more positive when the inhibitors are present, especially the CHDEPS3 inhibitor (from −197.39 to −0.537 J mol$^{-1}$ K$^{-1}$), indicating an enhanced protective effect on carbon steel following the addition of inhibitors. The elevated positive values of $\Delta H^*$ and diminished negative values of $\Delta S^*$ for inhibited solutions, relative to the blank solution, suggest that the presence of inhibitor molecules increases the energy level of the corrosion process. Therefore, it is reasonable to assume that the deposited inhibitor molecules raised the Fermi energy level of the carbon steel surface. Additionally, the calculated enthalpy and entropy values indicate that the organic inhibitors are sufficient as corrosion inhibitors on the surface of carbon steel, ranked in the following order: CH-DEPS3 > CH-DEPS2 > CH-DEPS1 > CH, as shown in Table 6.

**3.7.3. Adsorption isotherm parameters.** The interaction between the inhibitor and the metal surface was investigated using various adsorption isotherm models (Langmuir, El-Awady, and Flory–Huggins). By fitting surface coverage data to these equations, the specific isotherm that best described the experimental results was identified to define the adsorption process. The most suitable adsorption model was determined by evaluating the regression coefficient ($R^2$) obtained from the linear plots of each isotherm, see Fig. 15.

Langmuir isotherm:[70]

$$C/\theta = 1/K_{ads} + C \quad (10)$$

Flory–Huggins isotherm:[71]

$$\log[\theta/C] = \log K_{ads} + x \log(1 - \theta) \quad (11)$$

El-Awady isotherm:[72]

$$\log[\theta/(1 - \theta)] = \log K' + Y \log C \quad (12)$$

As displayed in Fig. 15, Langmuir isotherm model is considered the best suitable fitted data, as well as the linear regression coefficients of the Langmuir adsorption isotherm are near unity, indicating that the adsorption of the inhibitors on the mild steel surface in a 1.0 M HCl solution follows the Langmuir adsorption isotherm. The slope of the linear plot was determined to be 0.998, a value nearly equal to the theoretical ideal of unity (nearly 1). Equilibrium constant $K_{ads}$ value provides an indicator of the strength of the adsorption capacity between the prepared inhibitors, CH and CHDEPS1-3 inhibitors, and the carbon steel surface. This parameter can be performed using the following equation:

$$G^{\circ}_{ads} = RT \ln(55.5K_{ads}) \quad (13)$$

The values of $K_{ads}$ (M$^{-1}$) and $G^{\circ}_{ads}$(kJ mol$^{-1}$) have been presented in Table 7. The elevated $K_{ads}$ values of 6250, 16 129, 35 714, and 37 453 M$^{-1}$ for CH, CHDEPS1, CHDEPS2, and CHDEPS3, respectively, indicate a significant adsorption interaction between the selected inhibitors and the carbon steel surface in the aggressive 1.0 M HCl solution, particularly for the CHDEPS3 inhibitor.

Additionally, this finding aligns with the results from electrochemical measurements. Furthermore, the negative value of $\Delta G^{\circ}_{ads}$ indicates that the layer of adsorbed inhibitor is in a more stable state or possesses lower free energy compared to its state prior to adsorption.[73] The determined$\Delta G^{\circ}_{ads}$ values for the CH, CHDEPS1, CHDEPS2, and CHDEPS3 inhibitors were −31.60, −33.95, −35.92, and −36.04 kJ mol$^{-1}$, respectively, all of which are less negative than −40 kJ mol$^{-1}$. As a result, the adsorption of these organic inhibitors corresponds to the equivalence of the chemisorption and physisorption processes.

The chemisorption process arises from the presence of various heteroatoms (O, N, and S) within the structure of inhibitors, which facilitate interactions with the vacant orbitals of metals through lone pairs.[74] Conversely, the physisorption process arises from the increased presence of aromatic rings within the structure, particularly in the case of the CHDEPS3 inhibitor. The carbon steel surface undergoes oxidation to

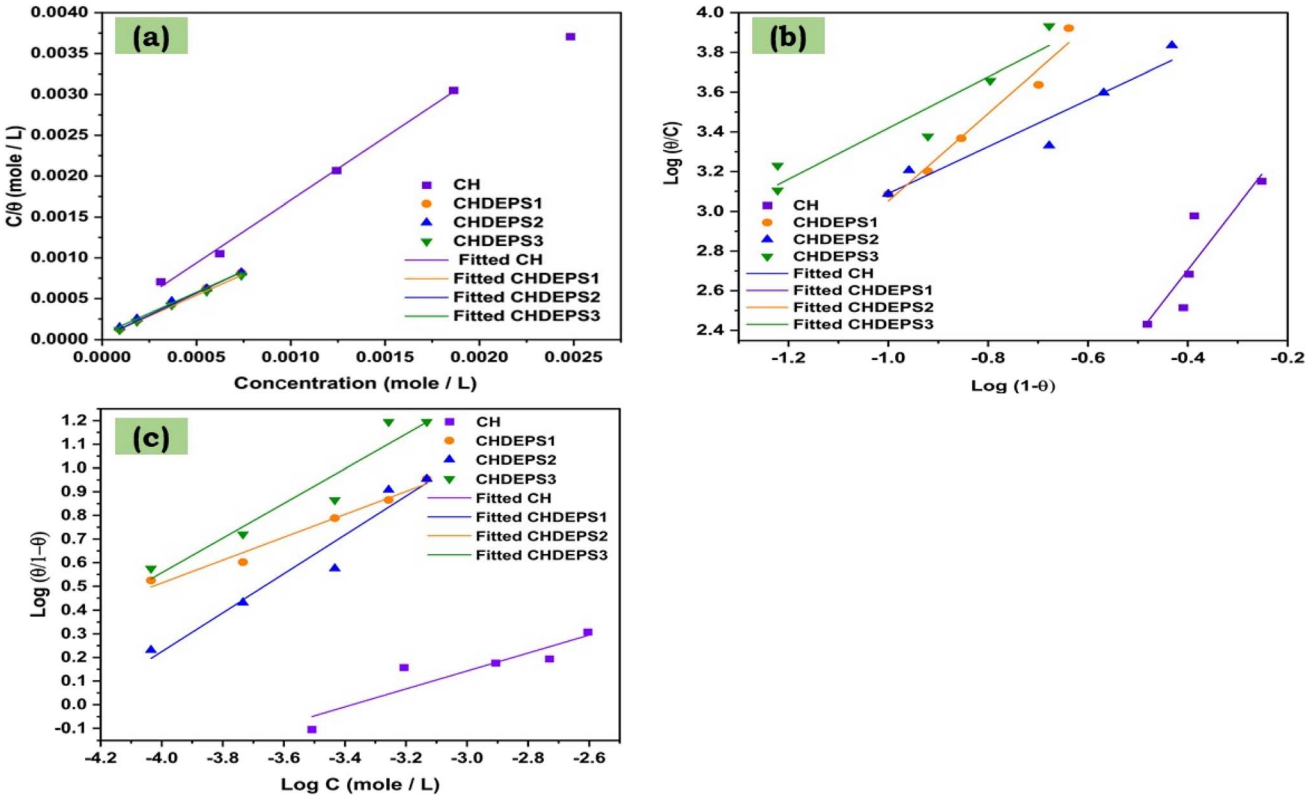


Fig. 15 Adsorption isotherm models for the adsorption of the samples on the carbon steel surface (a) Langmuir, (b) Flory–Huggins, and (c) El-Awady isotherm.

generate a positively charged surface upon exposure to the HCl solution rich in $Cl^-$ ions, facilitating the pre-adsorption of $Cl^-$ ions. The recent inhibitors are subjected to protonation in an acidic environment, subsequently engaging in physical adsorption due to electrostatic interactions with the pre-adsorbed $Cl^-$ ions. The inhibitor molecules approach the steel surface at a closer distance because of this phenomenon, which enables charge transfer to begin. The protonated inhibitor molecules may revert to their neutral state, thereby forming a coordinate bond and releasing hydrogen gas, by transferring electrons to the carbon steel surface. When electrons from the benzene ring and the lone pairs of heteroatoms move to the unoccupied d-orbitals of a metal alloy, chemical adsorption occurs.[75] Finally, the observed data confirmed that the modified chitosan inhibitors align with the Langmuir isotherm model, which is carried out by a mixed type of adsorption and is regarded as an effective organic inhibitor; furthermore, the CHDEPS3 inhibitor stands out as the most effective among them.

Table 7 Adsorption isotherm parameters for 400 ppm concentration of chitosan and their modified chitosan sulfonamide onto low carbon steel in 1.0 M HCl at 298 K

| Inhibitor | Slope | $R^2$ | Intercept | $K_{ads}$ ($M^{-1}$) | $-\Delta G$ (kJ $mol^{-1}$) |
|---|---|---|---|---|---|
| CH | 1.53 | 0.998 | $1.6 \times 10^{-4}$ | 6250 | 31.60 |
| CHDEPS1 | 1.03 | 0.997 | $6.2 \times 10^{-5}$ | 16 129 | 33.95 |
| CHDEPS2 | 1.02 | 0.999 | $2.8 \times 10^{-5}$ | 35 714 | 35.92 |
| CHDEPS3 | 1.08 | 0.999 | $2.67 \times 10^{-5}$ | 37 453 | 36.04 |

### 3.8. Mechanism corrosion and inhibition insights

The corrosion mechanism and corrosion inhibition mechanism using the synthesized organic inhibitors are demonstrated *via* the adsorption process and displayed in Fig. 16. As shown in the mentioned figure, the presence of a chloride medium may accelerate the corrosion process of Fe. In the initial phase, chloride ions ($Cl^-$) from the medium are adsorbed onto the Fe surface, as indicated in eqn (11). Electrostatic interactions between oppositely charged layers, such as those between positively charged Fe atoms and negatively charged $Cl^-$, enhance adsorption. Consequently, $Fe^{2+}$ or $Fe^{3+}$ is generated at the anodic site through the loss of electrons, as illustrated in eqn (14)–(16).[76]

$$Fe[(H_2O)_n]_{ads} + Cl^- \leftrightarrow Fe[(H_2O)_nCl]_{ads} + e^- \quad (14)$$

$$Fe[(H_2O)_nCl]_{ads} \leftrightarrow Fe^{2+} + nOH^- + nOH^+ + Cl^- + e^- \quad (15)$$

$$Fe^{2+} \leftrightarrow Fe^{3+} + e^- \quad (16)$$

On the cathodic side, according to eqn (17)–(19), hydronium ions ($H_3O^+$) take electrons to form hydrogen ($H_2$) and water ($H_2O$).[77]

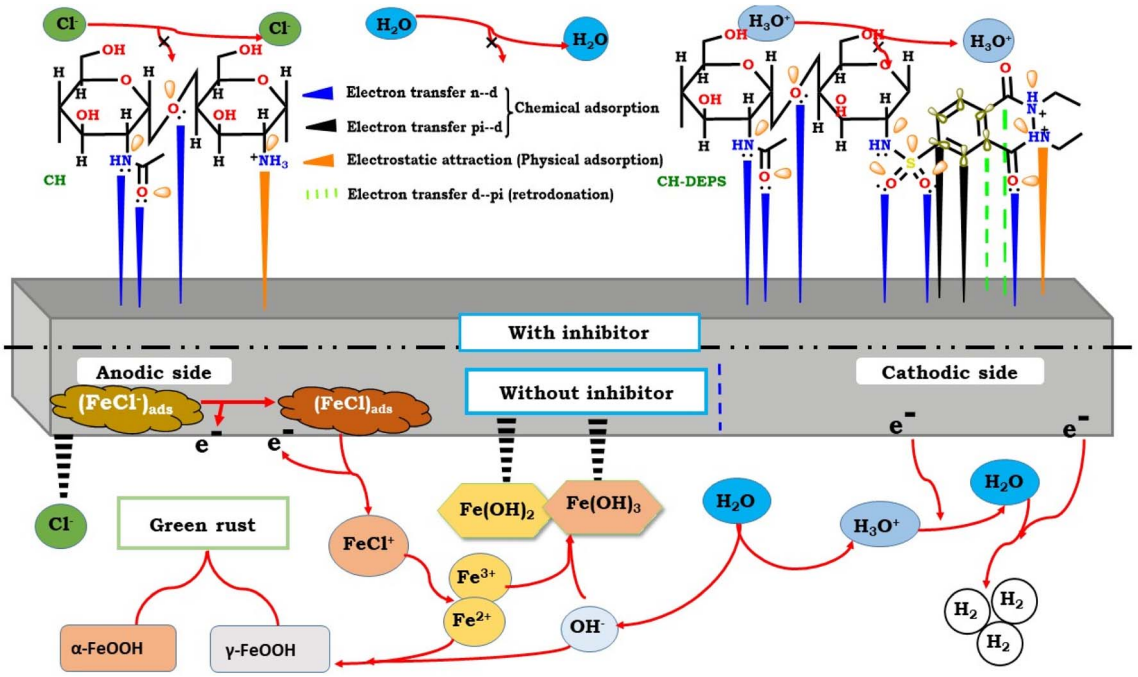


Fig. 16 Suggested corrosion mechanism and corrosion inhibition mechanism of the native CH and their modified sulfonamide CH-DEPS.

$$M + H_3O^+ \leftrightarrow M(H_3O)_{ads}^+ \quad (17)$$

$$M(H_3O)_{ads}^+ \leftrightarrow M(H_3O)_{ads} + e^- \quad (18)$$

$$M(H_3O)_{ads} + e^- + H^+ \leftrightarrow M + H_2O + H_2 \quad (19)$$

The resulting corrosive products comprise predominantly ferrous hydroxide ($Fe(OH)_2$), ferric hydroxide ($Fe(OH)_3$), goethite (α-FeOOH), and lepidocrocite (γ-FeOOH). In reference to the final two, they are designated as 'green rust'. Adding chloride molecules to the corrosive electrolyte has a significant influence on corrosion. Chloride molecules form a protective film at the metal-electrolyte interface, preventing corrosive species, such as $Cl^-$, $H_2O$, and $H_3O^+$, from reaching the metal exterior.

Generally, the development of the shielding adsorption film can be attributed to the adsorption mechanism, which includes physisorption and retro-donation between the inhibitors and the intended surface. This process is enhanced by the presence of aromatic rings, unsaturated bonds, heteroatoms, and polar groups such as $-SO_2$, –N-alkyl and C═O.[66] The recent chemical inhibitors exhibited an adsorption process consistent with the adsorption phenomenon. In this instance, it is noted that the modified chitosan sulfonamide structure, CHDEPS, exhibited an inhibition mechanism that was better and slightly different from that of the native chitosan, CH (Fig. 14). The presence of polar functions, such as $-NH_2$ and –OH, enhances the surface coverage of the underlying metal plane. Nevertheless, the native CH inhibitor exhibited only two types of adsorptions; the first adsorption involved electron transfer from the heteroatoms to the free orbital of the metal n–d, which was identified as chemical adsorption. The second type involved the electrostatic attraction between protonated polar functions and the negative chloride ion on the surface. Moreover, the CHDEPS structure comprises two aromatic rings, π-bonding orbitals, electron-rich heteroatoms (O, N, and S), polar groups (–NH and C═O), and planar structures in CIs, which enhance the surface coverage of the metal plane compared to native chitosan. Overall, the adsorption of the CH-DEPS organic inhibitors on the alloy's surface encompasses two classes of chemical adsorption—namely, electron transfer from the lone pair of hetero atoms to the free orbital of metal (n–d) and electron transfer from π-bonding orbitals of aromatic rings to the free orbital of metal (pi–d). Alongside physical adsorption characterized by electrostatic attraction, as well as the retrodonation process involving electron transfer from d–pi (Fig. 16). The enhanced electron donation property and different inhibition process in the CHDEPS structure led to an improved adsorption capability, which is subsequently reflected in the superior surface protection property than the native chitosan CH.

### 3.9. Comparison with other organic inhibitors

To situate the current investigation, this section compares the prepared inhibitors, CHDEPS1-3, with well-cited organic corrosion inhibitors from the existing literature. The comparison is based on structural characteristics, optimum dose, corrosive medium, and inhibition efficiency. As detailed in Table 8, our inhibitors were assessed against reported compounds that share structural similarities. Table 8 lists previously published work based on phthalazine derivative compounds and previously published work based on modified chitosan derivatives. In addition, the chemical structure of our inhibitors in this study involved a combination of chitosan and phthalazine *via* sulfonamide function. The results show that the inhibitors in this study possess acceptable and competitive corrosion inhibition efficiencies (98.4%), which is comparable to the reported previous inhibitors (maximum 95.2%). The

Table 8 Presents a selection of well-cited literature on organic corrosion inhibitors for comparison with the current investigation

| Organic inhibitors | Substrate | Concentration | Efficiency (IE%) | Ref. |
|---|---|---|---|---|
| 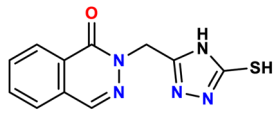 I | | | 71.7%% | |
| 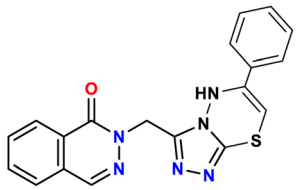 II | | | 76.5% | |
| 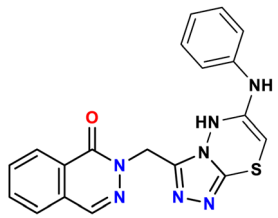 III | 1.0 M $H_2SO_4$, copper | 60 μM $L^{-1}$ | 80.6% | 32 |
| 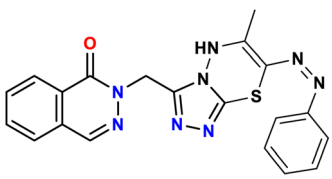 IV | | | 84.3% | |
| 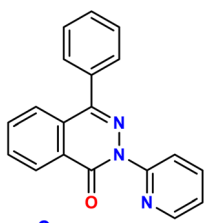 2c | | | 93.4% | |
| 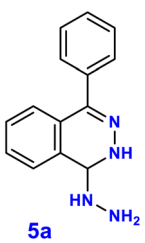 5a | 5.0 M HCl, steel coupons | 0.02 M | 47.8% | 34 |
| 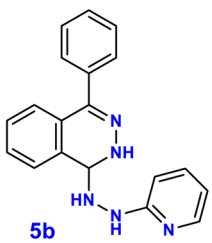 5b | | | 57.1% | |
| | | | 64.3% | |

Table 8 (*Contd.*)

| Organic inhibitors | Substrate | Concentration | Efficiency (IE%) | Ref. |
|---|---|---|---|---|
| 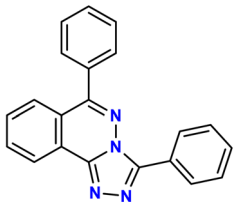 7 | 0.5 M $H_2SO_4$, low carbon steel | 0.5 mM | 88% | 78 |
| 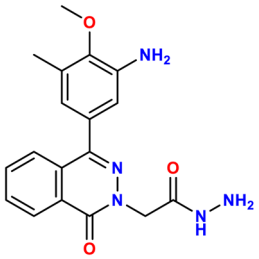 APPH | | | | |
| 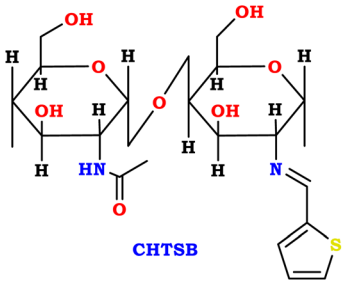 CHTSB | 1 mol $L^{-1}$ HCl, mild steel | 1500 ppm | 92% | 27 |
| 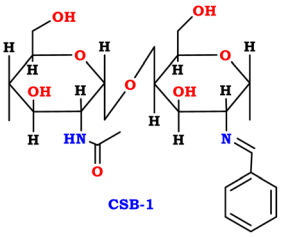 CSB-1 | | | 84.5% | |
| 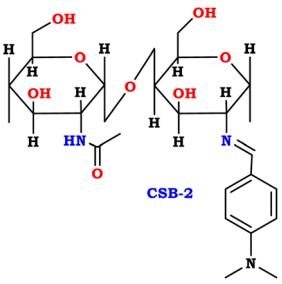 CSB-2 | 1.0 M HCl, mild steel | 50 mM | 87.2% | 28 |
| | | | 91.9% | |

Table 8 (*Contd.*)

| Organic inhibitors | Substrate | Concentration | Efficiency (IE%) | Ref. |
|---|---|---|---|---|
| 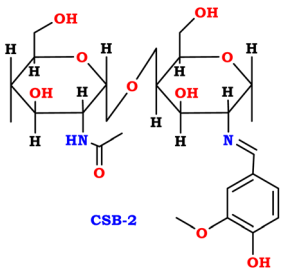 CSB-2 | 3.5% NaCl saturated with carbon dioxide | 150 mg $L^{-1}$ | 95.2% | 29 |
| 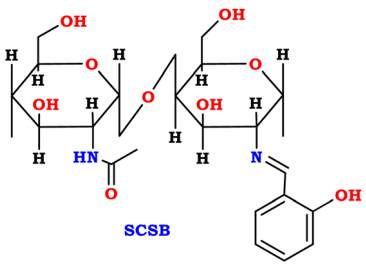 SCSB | | | | |
| 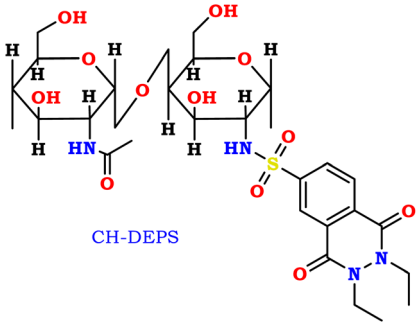 CH-DEPS | 1.0 M HCl, low carbon steel | 400 ppm | 98.48% | Present study |

results confirm that this work is a reasonable and practical extension of modified chitosan as a green corrosion inhibitor. Finally, the results obtained indicate that this recent work is a reasonable extension of the work on modified chitosan inhibitors.

### 3.10. Theoretical calculation studies

**3.10.1. Frontier molecular orbitals and global reactivity descriptors.** The optimized molecular structures of chitosan CH and modified chitosan sulfonamide CH-DEPS are shown schematically in Fig. 17a, along with their frontier molecular orbitals (FMOs) in Fig. 17b. The HOMO and LUMO density distributions indicate the likely reactive sites of the inhibitor molecules. In CH, the HOMO is mainly localized on the lone pair orbitals of O and N (glucosamine units), whereas the LUMO of CH is primarily located around the glycosidic linkages and the electron-rich heteroatoms (O and N). In contrast, the CH-DEPS structure shows HOMO delocalization shifts toward the newly attached heterocyclic moieties, particularly focused on the N atoms within the aromatic heterocycle, and its LUMO distribution prominently spans the aromatic sulfonamide-based substituent. The π-conjugated aromatic ring and adjacent heterocyclic N atoms significantly contribute to the LUMO electron density. Both molecules' HOMO orbitals are associated with electron-donating ability (to empty metal orbitals), whereas the LUMO can accept electron density from the metal surface *via* back-donation. This broad delocalization in the chemically modified CHDEPS is directly attributed to the introduction of π-conjugation and additional heteroatoms, greatly enhancing chemisorption strength and electron-transfer capability. The distribution of these orbitals suggests that the heteroatoms (O, N, S) are the primary adsorption centers, as these atoms contribute strongly to the HOMO electron cloud in inhibitors (and also to LUMO in terms of antibonding orbitals that can accept electrons).

On the other hand, the DFT-calculated frontier orbital energies (HOMO/LUMO) and associated global descriptors for CH and CHDEPS are shown in Table 9. The results confirm that CHDEPS is more favorable for adsorption electronically. CH-DEPS exhibits a higher HOMO energy (less negative) and

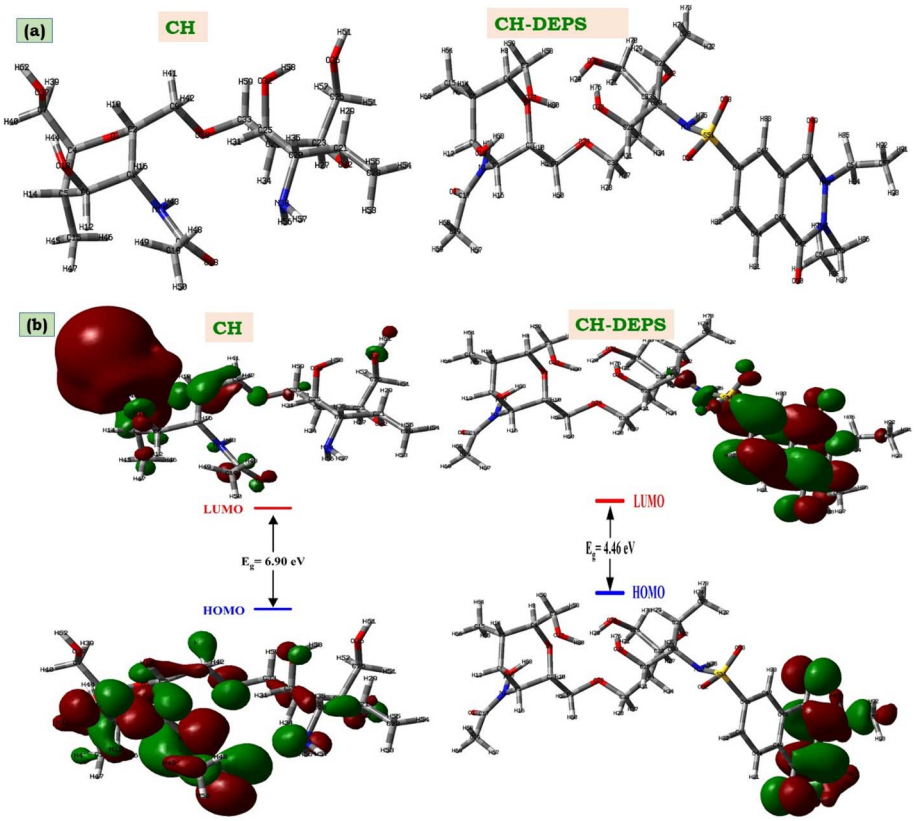


Fig. 17 (a) Optimized molecular structures and (b) frontier molecular orbitals (HOMO/LUMO) of CH and CH-DEPS inhibitors.

a lower LUMO energy than CH, resulting in a smaller HOMO–LUMO energy gap ($\Delta E$).[79] This narrower gap (4.03 eV in CHDEPS compared to 6.90 eV in CH) suggests that CH-DEPS is more chemically reactive and capable of accepting electrons more readily than CH, thereby enhancing its interaction with the metal surface. The smaller $\Delta E$, increased electron affinity, higher softness, and electrophilicity of CHDEPS explain its superior experimentally observed inhibition efficiency. This molecular-level understanding aligns seamlessly with experimental electrochemical findings, confirming that CHDEPS should interact more strongly with the steel surface and is considered an excellent corrosion inhibitor compared to unmodified CH. All these parameters consistently indicate that CHDEPS should interact more strongly with the steel surface than CH, which aligns with the experimental finding of its superior inhibition efficiency.

On the other hand, the electrostatic potential (ESP) maps offer a complementary view of the molecular charge distribution in real space. Fig. 18 depicts the mapped ESP surfaces for CH and CHDEPS. Negative (red-orange) regions denote electron-rich nucleophilic centers; positive (blue-green) regions represent electron-deficient electrophilic sites. Both molecules exhibit regions of negative potential (colored red) in the vicinity of heteroatoms (O, N, and S), as expected since these atoms carry lone pairs and partial negative charges. In CH (Fig. 17a), the most negative ESP regions are around the amine N and the ring O atoms. CH-DEPS (Fig. 17b) shows a broadly similar pattern, but the introduction of the DEPS group creates additional negative potential sites, especially around the imine N atoms (C=N–) and any aromatic substituents. The ESP map of CH-DEPS is more "polarized," consistent with its increased dipole moment (CH ~6.54 D; CH-DEPS ~7.14 D) and the presence of strongly electron-donating groups.[80,81] The more extended red regions on CH-DEPS imply that when this molecule approaches a positively charged metal surface, it can establish electrostatic attraction over a larger surface area, aiding its anchoring. In summary, CH-DEPS provides more and stronger negative potential sites than CH, facilitating stronger electrostatic attraction and multidentate adsorption on the Fe surface. This factor contributes to the higher inhibition

Table 9 Quantum chemical reactivity descriptors for CH and CH-DEPS inhibitors

| Descriptor | $E_{HOMO}$ | $E_{LUMO}$ | $\Delta E$ | $I$ | $\chi$ | $\eta$ | $\sigma$ | $\mu$ | $\omega$ | $E_a$ |
|---|---|---|---|---|---|---|---|---|---|---|
| CH | −5.85 | −1.05 | 6.90 | 5.85 | 2.40 | 3.45 | 0.14 | −2.40 | 0.83 | −1.05 |
| CH-DEPS | −6.23 | −2.20 | 4.03 | 6.23 | 4.22 | 2.01 | 0.25 | −4.22 | 4.42 | 2.20 |

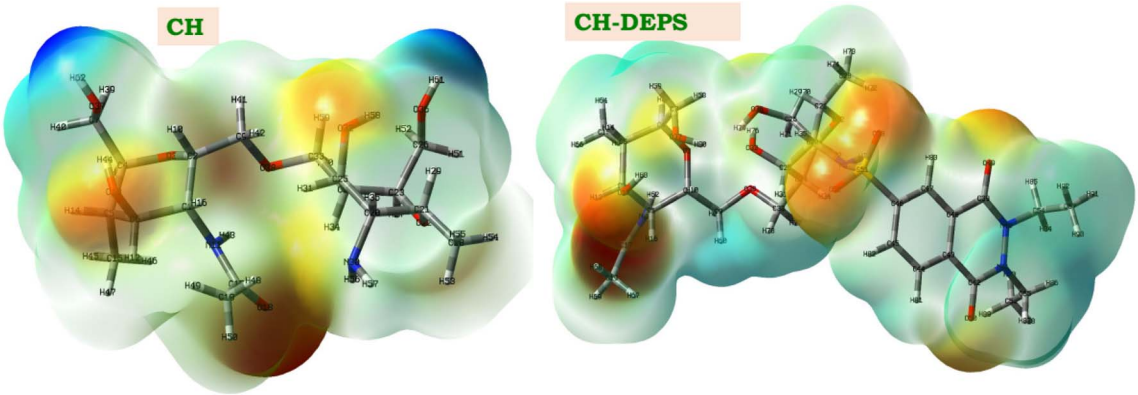


Fig. 18 ESP graphic maps of CH, and CHDPES materials.

efficiency of CH-DEPS, as a closely bound and extensive inhibitor film will more effectively block the Fe surface from corrosive species.

**3.10.2. Monte Carlo simulation.** To simulate the adsorption process of the inhibitors on the Fe(110) surface, Monte Carlo (MC) simulations using the adsorption locator were performed in both gas and aqueous conditions. Both CH and CHDEPS consistently converged to configurations where the molecules lie nearly flat on the Fe(110) surface, maximizing their contact area (Fig. 19). This parallel orientation is commonly observed for large inhibitors, as it allows multiple adsorption sites to engage with the surface. In our case, chitosan tends to adsorb *via* its ring O and $NH_2$ facing the surface (with the polymer backbone somewhat flattened), whereas CHDEPS adsorbs with its entire DEPS moiety and the chitosan units all near the metal – essentially a "flat" conformation that enables all heteroatoms to interact with Fe if possible.[82] The adsorption behavior of CH and CHDEPS molecules onto the Fe(110) surface in gas-phase and simulated acidic solution-phase conditions was investigated using Monte Carlo simulations, as shown in Fig. 18. The adsorption energies ($E_{ads}$), rigid adsorption energies ($E_{rigid}$), and deformation energies ($E_{def}$) are shown in Table 10.

Both CH and CHDEPS show significantly negative adsorption energies, indicating spontaneous and energetically favorable adsorption processes. Notably, CHDEPS exhibits considerably more negative adsorption energies ($-356.01$ kcal mol$^{-1}$ in gas-phase and $-1873.91$ kcal mol$^{-1}$ in aqueous-phase) than CH ($-214.43$ kcal mol$^{-1}$ in gas-phase and $-1772.51$ kcal mol$^{-1}$ in aqueous-phase). The deformation energies ($E_{def}$) confirm structural relaxation upon adsorption, which is more pronounced for the aqueous phase, suggesting stronger and more effective interaction with the metal surface (Table 10).

**3.10.3. Molecular dynamics simulations.** MD simulations provide dynamic insight into how the inhibitor films behave,

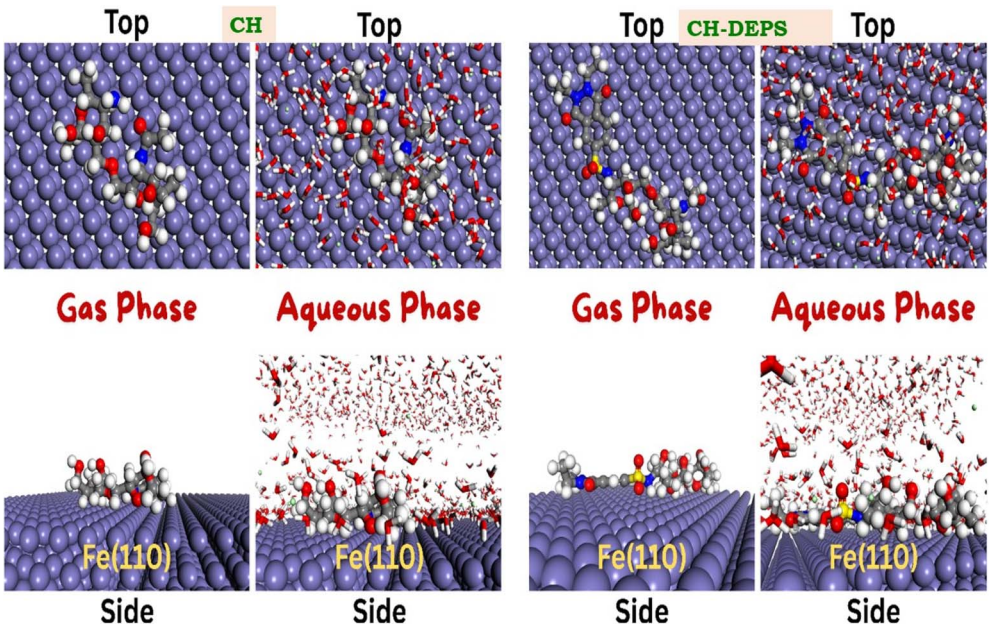


Fig. 19 MC adsorption configurations of CH and CH-DEPS inhibitors on the Fe(110) in gas and aqueous phases.

Table 10 MC simulation results for adsorption of CH and CH-DEPS on Fe(110)

| Conditions | Structure | Total energy (kcal mol$^{-1}$) | $E_{ads}$ (kcal mol$^{-1}$) | $E_{rigid}$ (kcal mol$^{-1}$) | $E_{def}$ (kcal mol$^{-1}$) |
|---|---|---|---|---|---|
| Gas phase | CH | −189.61 | −214.43 | −191.13 | −23.30 |
| Aqueous phase | CH-DEPS | −334.25 | −356.01 | −323.00 | −33.01 |

especially over time and at different temperatures. We carried out MD simulations for CH and CHDEPS at 298 K. The MD trajectories clearly showed that both inhibitors adsorb quickly onto the Fe(110) surface and remain adsorbed throughout the simulation (50 ps). However, differences were observed in their behavior under thermal agitation. MD simulations further elucidate the stability of adsorbed inhibitor films on the Fe surface through temperature equilibrium analysis at 298 K (Fig. 20a). After initial fluctuations, both inhibitors quickly reached stable equilibrium, maintaining consistent temperature profiles. The steady-state stability of CHDEPS is particularly evident, indicating a stable inhibitor layer formation with minimal fluctuations, conducive to effective corrosion protection.

To analyze the structural arrangement of the adsorbed molecules, we computed radial distribution functions (RDFs) between the metal surface atoms and the inhibitor's key atoms (O, N, and S). Fig. 19b shows, for each inhibitor, the RDF $g(r)$ of Fe–O (red curve), Fe–N (blue curve), and Fe–S (yellow curve) at 298 K. The RDF analysis from MD simulations provides insight into atom-specific interaction distances between the inhibitor molecules and the Fe(110) surface (Fig. 20). Knowing that the peak between 1 and 3.5 Å corresponds to chemisorption and that physisorption is associated with peaks greater than 3.5 Å.[83] For CH, the RDF analysis reveals that O and N atoms predominantly interact with Fe at short distances (2.81 Å for O and 3.17 Å for N), confirming effective adsorption.[84] For CHDEPS, O, N, and S atoms interact at distances of 2.89 Å, 3.35 Å, and 3.43 Å, respectively, demonstrating a multifunctional adsorption capability due to the presence of additional heteroatoms and aromatic rings. These short-range interactions underline strong chemical adsorption mechanisms that stabilize the inhibitor–metal interface. These RDFs confirm that CHDEPS forms more numerous and tighter Fe–O/N/S bonds (chemisorption range) than chitosan, which correlates with CHDEPS's higher surface coverage and inhibition effectiveness.

A direct correlation exists between the calculated theoretical parameters (such as bandgap, ESP distribution, electrophilicity, and electronic transitions) and the experimentally measured corrosion inhibition performance.[85–87] Specifically, CHDEPS, with superior electronic properties, experimentally shows significantly higher corrosion inhibition efficiency (up to ~94%) compared to CH. Both MC and MD analyses confirm the feasibility and stability of inhibitor adsorption, supporting

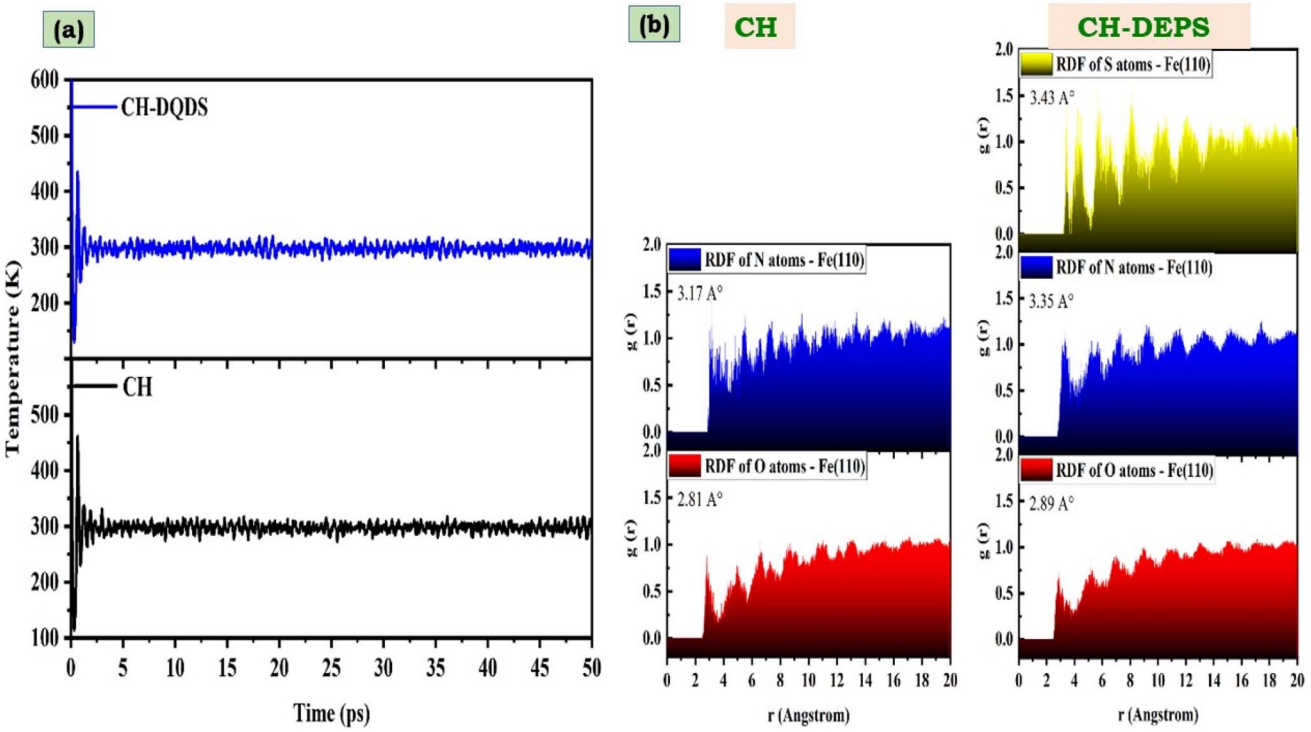


Fig. 20 (a) Temperature equilibrium curves (298 K). (b) RDF plots indicating chemisorption interactions between heteroatoms (N, O, S) and Fe(110).

experimental observations. The significantly more negative $E_{ads}$ values for CHDEPS in both gas and solution phases, the stable temperature profiles, and the close interaction distances (RDF analysis) substantiate the experimentally higher corrosion inhibition efficiency for CHDEPS. Specifically, the robust adsorption of CHDEPS, evidenced by simulation, aligns precisely with its experimentally superior inhibition efficiency (~94%).

# 4 Conclusion

This study involved the synthesis of a sulfonamide conjugate derived from chitosan, with the objective of altering its chemical structure. The incorporation of the 1,4-pthalazinedione moiety was intended to improve the properties of chitosan, yielding a more versatile and efficient derivative for diverse environmental applications. A modified chitosan sulfonamide was created through the condensation reaction of a newly synthesized phthalazine-6-sulfonyl chloride derivative, DEPS, and chitosan, CH. Several techniques, including $^{1}$H NMR, $^{13}$C NMR, FTIR, SEM, and XRD, were employed to analyze the derivatives. The formation of the modified-chitosan sulfonamide induced significant structural modifications in chitosan, improving its morphological properties. In addition, the maximum degree of substitution recorded was 0.44, which correlated with the highest molar ratio of the phthalazine-6-sulfonyl chloride derivative (DEPS).

The incorporation of the 1,4-pthalazinedione moiety has been observed to significantly enhance the anticorrosion properties of chitosan. This enhancement is successful for a low-carbon steel sample in a 1.0 M HCl solution. The modified sulfonamide conjugate has exhibited significantly enhanced corrosion inhibition efficiency in comparison to the native chitosan. The electrochemical assessments indicate that the CHDEPS3 formulation exhibits remarkable corrosion inhibition capabilities for CS in an acidic environment, achieving inhibition efficiencies of 95.38% at a concentration of 400 ppm, compared to 72% for the native chitosan. CH-DEPS3 shows potential as an eco-friendly, effective anticorrosion inhibition material for CS, which depends on the molar ratio of 1,4-pthalazinedione incorporated.

The surface characterization of the CS sample, including SEM-EDX mapping and AFM analysis, indicates that the CH-DEPS3 inhibitor was highly uniformly dispersed on the surface of the sample through its dissolution in the corrosive medium (HCl solution) and subsequent absorption to create a protective layer on the steel. Quantum chemical calculations indicate that the incorporation of a 1,4-pthalazinedione enhances the electron transfer capability and hydrophobicity of CHDEPS compared to CH, thereby promoting the adsorption of CHDEPS molecules on the CS surface. MC/MD simulations indicate that CHDEPS molecules adsorbed on the CS surface in a planar fashion by establishing covalent bonds. A film of adsorbed CHDEPS could effectively impede the diffusion of aggressive species.

Ultimately, this study presents a concept for the development and application of environmentally sustainable modified chitosan sulfonamides in mitigating the corrosion of carbon steel. Such an approach can be used to screen and optimize inhibitor molecules before synthesis, accelerating the development of effective and sustainable corrosion mitigation solutions.

# Conflicts of interest

The authors declare that they have no conflict of interest.

# Abbreviations

| | |
|---|---|
| DEP | 2,3-Diethyl-2,3-dihydrophthalazine-1,4-dione |
| DEPS | 2,3-Diethyl-1,4-dioxo-1,2,3,4-tetrahydrophthalazine-6-sulfonyl chloride |
| CHDEPS1 | Chitosan and different molar ratios of DEPS materials |
| CS | Carbon steel sample |
| MS | Mild steel sample |
| FTIR | Fourier transform infrared spectroscopy |
| AFM | Atomic force microscope |
| $^{1}$H NMR | Proton nuclear magnetic resonance |
| SEM | Scanning electron microscopy analysis |
| EDX | Energy-dispersive X-ray analysis |
| XRD | X-ray diffraction |
| DS | Degree of substitution |
| EIS | Electrochemical impedance spectroscopy |
| PDP | Potentiodynamic polarization analysis |
| $\eta_{EIS}$ | Inhibition efficiency |
| CR | Corrosion rate measured |
| DFT | Density functional theory |
| TD-DFT | Time-dependent density functional theory |
| $\Delta E$ | Bandgap energy |
| $A$ | Electron affinity |
| $I$ | Ionization potential |
| $\eta$ | Chemical hardness |
| $\sigma$ | Softness |
| $\chi$ | Electronegativity |
| $\omega$ | Electrophilicity |
| $\mu$ | Chemical potential |

# Data availability

Data will be made available on request.

# Acknowledgements

The authors extend their appreciation to Northern Border University, Saudi Arabia, for supporting this work through project number (NBU-CRP-2025-128).

# References

1 G. P. V. Dalmora, E. P. Borges Filho, A. A. M. Conterato, W. S. Roso, C. E. Pereira and A. Dettmer, *Results Surf. Interfaces*, 2025, 100430.

2 G. A. Abd-elmaksoud, M. S. Abusaif, Y. A. Ammar, S. Al-Sharbasy and M. A. Migahed, *Arabian J. Sci. Eng.*, 2023, **48**, 16167–16185.
3 A. C. Njoku, S. C. Nwanonenyi, P. I. Anyanwu, B. I. Onyeachu, I. O. Eze, M. N. Akanbi, C. K. Oguzie and D. I. Njoku, *J. Build. Eng.*, 2025, **106**, 112602.
4 M. S. Abusaif, A. M. Hyba, Y. A. Ammar, M. A. Salem, D. M. Elsisi and A. Ragab, *J. Taiwan Inst. Chem. Eng.*, 2023, **153**, 105207.
5 G. Ghenimi, N. Ferraa, H. Barebita, T. Guedira and M. Cherkaoui, *Moroccan J. Chem.*, 2025, **13**, 440–458.
6 S. L. Gaonkar, D. Nayak, P. P. Kumari, J. N. Mishma, D. Dwarakanath, S. A. Rao and P. Bhagavath, *J. Bio Tribo Corros.*, 2025, **11**, 1–20.
7 O. Gharbi, S. Thomas, C. Smith and N. Birbilis, *npj Mater. Degrad.*, 2018, **2**, 12.
8 B. El Ibrahimi, A. Jmiai, L. Bazzi and S. El Issami, *Arab. J. Chem.*, 2020, **13**, 740–771.
9 W. Emori, H. Louis, P. C. Okonkwo, D. I. Njoku, H. O. Edet, P. C. Okafor and C.-R. Cheng, *Sustain. Chem. Pharm.*, 2023, **32**, 101042.
10 D. I. Njoku, C. N. Njoku, H. Lgaz, P. C. Okafor, E. E. Oguzie and Y. Li, *J. Mol. Liq.*, 2021, **330**, 115619.
11 C. A. Maduabuchi, D. I. Njoku, O. I. Anthony, S. C. Nwanonenyi, C. Akalezi, A. Blessing and E. E. Oguzie, *Electroanalysis*, 2020, **32**, 3117–3130.
12 Y. L. Kobzar and K. Fatyeyeva, *Chem. Eng. J.*, 2021, **425**, 131480.
13 H. Ashassi-Sorkhabi and A. Kazempour, *Carbohydr. Polym.*, 2020, **237**, 116110.
14 D. I. Njoku, E. E. Oguzie and Y. Li, *J. Mol. Liq.*, 2017, **237**, 247–256.
15 M. H. Shahini, B. Ramezanzadeh and H. E. Mohammadloo, *J. Mol. Liq.*, 2021, **325**, 115110.
16 R. C. Nascimento, L. B. Furtado, and M. J. O. C. Guimarães, in *Grafted Biopolymers as Corrosion Inhibitors: Safety, Sustainability, and Efficiency*, 2023, pp. 21–55.
17 P. Mahajan and M. Sharma, *Energy Storage*, 2024, **6**, e634.
18 N. Er-rahmany, M. Nounah, S. Yaqouti, A. Nounah, R. Touir and E. H. El Kafssaoui, *Next Res.*, 2025, **2**, 100148.
19 E. Berdimurodov, D. K. Verma, A. Kholikov, K. Akbarov and L. Guo, *J. Mol. Liq.*, 2022, **349**, 118124.
20 N. Errahmany, M. Rbaa, A. S. Abousalem, A. Tazouti, M. Galai, E. H. El Kafssaoui, M. E. Touhami, B. Lakhrissi and R. Touir, *J. Mol. Liq.*, 2020, **312**, 113413.
21 J. Du, X. Fan, D. Xiao, W. Wang, Y. Yin, Z. Li, K. He, Y. Tan, J. Yan and G. Liu, *Surf. Coating. Technol.*, 2024, **476**, 130211.
22 R. Drevet, J. Fauré and H. Benhayoune, *Coatings*, 2024, **14**, 1084.
23 M. A. Abu-Saied, M. A. Rafea, E. A. El Desouky, A. M. Ahmed and M. S. Abusaif, *ACS Omega*, 2025, **10**(23), 24950–24960.
24 B. Layek, S. Das and S. Paul, in *Tailor-Made and Functionalized Biopolymer Systems*, Elsevier, 2021, pp. 115–154.
25 A. Zarrouk, M. Messali, H. Zarrok, R. Salghi, A. A.-S. Ali, B. Hammouti, S. S. Al-Deyab and F. Bentiss, *Int. J. Electrochem. Sci.*, 2012, **7**, 6998–7015.
26 M. Galai, K. Dahmani, M. E. Touhami, R. Hsissou, F. Benhiba, M. Rbaa, M. Ouakki, R. Lachhab and S. M. Alharbi, *Mater. Sci. Eng., B*, 2023, **298**, 116843.
27 R. Menaka and S. Subhashini, *Polym. Int.*, 2017, **66**, 349–358.
28 J. Haque, V. Srivastava, D. S. Chauhan, H. Lgaz and M. A. Quraishi, *ACS Omega*, 2018, **3**, 5654–5668.
29 K. R. Ansari, D. S. Chauhan, M. A. Quraishi, M. A. J. Mazumder and A. Singh, *Int. J. Biol. Macromol.*, 2020, **144**, 305–315.
30 C. Verma, D. K. Verma, E. E. Ebenso and M. A. Quraishi, *Heteroat. Chem.*, 2018, **29**, e21437.
31 S. K. Saha, P. Ghosh, A. Hens, N. C. Murmu and P. Banerjee, *Phys. E*, 2015, **66**, 332–341.
32 S. A. Abd El-Maksoud, *Electrochim. Acta*, 2004, **49**, 4205–4212.
33 H. Chkala, S. Ighir, W. Ettahiri, M. Taleb, M. Chigr and N.-E. El Mansouri, *Constr. Build. Mater.*, 2024, **428**, 136188.
34 M. M. Hemdan, S. M. Taha, A. M. Gabr and M. Y. Elkady, *J. Chem. Res.*, 2014, **38**, 617–621.
35 H. K. Thabet, A. Ragab, M. Imran, M. H. Helal, S. I. Alaqel, A. Alshehri, A. A. Mohd, S. S. Alshammari, Y. A. Ammar and M. S. Abusaif, *RSC Adv.*, 2024, **14**, 15691–15705.
36 N. A. Gohar, E. A. Fayed, Y. A. Ammar, O. A. Abu Ali, A. Ragab, A. M. Mahfoz and M. S. Abusaif, *J. Enzyme Inhib. Med. Chem.*, 2024, **39**(1), 2367128.
37 J. Nielsen and P. H. Rasmussen, *Tetrahedron Lett.*, 1996, **37**, 3351–3354.
38 A. Gangan, M. ElSabbagh, M. A. Bedair, H. M. Ahmed, M. El-Sabbah, S. M. El-Bahy and A. Fahmy, *Arab. J. Chem.*, 2021, **14**, 103391.
39 A. M. Abdel-karim, S. Shahen, D. M. Elsisi, A. M. Hyba and O. A. A. El-Shamy, *J. Bio Tribo Corros.*, 2022, **8**, 70.
40 J. R. Cheeseman and M. J. Frisch, *J. Chem. Theory Comput.*, 2011, **7**(10), 3323–3334.
41 A. D. Becke, *J. Chem. Phys.*, 1993, **98**, 5648–5652.
42 A. E. Hassan, A. M. Elewa, M. S. A. Hussien, A. F. M. El-Mahdy, I. M. A. Mekhemer, I. S. Yahia, T. A. Mohamed, H.-H. Chou and Z. Wen, *J. Colloid Interface Sci.*, 2024, **653**, 1650–1661.
43 J. H. Wang, A. E. Hassan, A. M. Elewa and A. F. M. EL-Mahdy, *J. Mater. Chem. A*, 2024, **12**, 14005–14021.
44 M. H. Helal, M. S. Abusaif, A. Ragab, S. Y. Abbas, R. Ayman, M. S. A. El-Gaby, S. A. Fouad and Y. A. Ammar, *Mol. Diversity*, 2025, 1–49.
45 N. A. Gohar, E. A. Fayed, Y. A. Ammar, O. A. Abu Ali, A. Ragab, A. M. Mahfoz and M. S. Abusaif, *J. Enzyme Inhib. Med. Chem.*, 2024, **39**, 2367128.
46 M. S. Abusaif, A. M. Sh El-Sharief, Y. A. Mohamed, Y. A. Ammar, M. A. Ismail, W. M. Aboulthana, M. S. A. El-Gaby and A. Ragab, *Sci. Rep.*, 2025, **15**, 19409.
47 M. A. Kadhim, M. G. Mukhlif, E. W. Gayadh, E. K. M. Zangana, M. A. Mohaisen, M. M. Matar and S. A. Rizk, *J. Mol. Struct.*, 2025, **1322**, 140384.
48 H. K. Thabet, M. S. Abusaif, M. Imran, M. H. Helal, S. I. Alaqel, A. Alshehri, A. A. Mohd, Y. A. Ammar and A. Ragab, *Comput. Biol. Chem.*, 2024, **111**, 108097.
49 D. M. Mamand, B. Y. Ahmed, D. M. Aziz, P. O. Hama, P. A. Mohammed, K. A. Abdalkarim, D. S. Muhammad,

A. M. Hussein, S. A. Hussen and S. B. Aziz, *Spectrochim. Acta, Part A*, 2025, **329**, 125485.
50 Z. Zhong, X. Ji, R. Xing, S. Liu, Z. Guo, X. Chen and P. Li, *Bioorg. Med. Chem.*, 2007, **15**, 3775–3782.
51 M. A. Abu-Saied, E. A. El Desouky, M. A. Rafea and M. S. Abusaif, *Mater. Today Commun.*, 2024, **40**, 110232.
52 C. Xie, I. Milošev, F. U. Renner, A. Kokalj, P. Bruna and D. Crespo, *J. Alloys Compd.*, 2021, **879**, 160464.
53 M. T. Ramesan, R. Gopika, T. T. K. Rahman, K. T. Jamsheena and B. K. Bahuleyan, *Int. J. Biol. Macromol.*, 2025, **309**, 142976.
54 G. A. Abd-elmaksoud, M. S. Abusaif, Y. A. Ammar, S. Al-Sharbasy and M. A. Migahed, *Arabian J. Sci. Eng.*, 2023, **48**, 16167–16185.
55 G. Özer, *Protect. Met. Phys. Chem. Surface*, 2022, **58**, 176–189.
56 C. N. Hippolyte, B. Y. Serge, A. Sagne, J. Creus and T. Albert, *J. Mater. Sci. Chem. Eng.*, 2018, **06**, 100–121.
57 A. M. Abdel-Gaber, B. A. Abd-El-Nabey, I. M. Sidahmed, A. M. El-Zayady and M. Saadawy, *Corros. Sci.*, 2006, **48**, 2765–2779.
58 M. A. Bedair, E. H. Alosaimi and S. Melhi, *J. Adhes. Sci. Technol.*, 2023, **37**, 105–135.
59 L. Guo, L. Zhu, S. Kaya, R. Sun, A. G. Ritacca, K. Wang and J. Chang, *Colloids Surf., A*, 2024, **702**, 135062.
60 M. R. Selim, M. A. Zahran, A. Belal, M. S. Abusaif, S. A. Shedid, A. B. M. Mehany, G. A. M. Elhagali and Y. A. Ammar, *Anticancer Agents Med. Chem.*, 2019, **4**, 439–452.
61 A. H. Elged, E. A. Ghiaty, N. M. El Basiony and S. M. Shaban, *J. Mol. Liq.*, 2025, **426**, 127297.
62 M. M. Y. Modwi, H. Feng, M. K. Hadi, N. Chen, J. Hou, E. Kamal and K. Yang, *J. Mol. Struct.*, 2025, **1321**, 139592.
63 A. Tomar, A. M. Khan, G. Ji and A. Sarkar, *J. Adhes. Sci. Technol.*, 2025, **39**, 615–634.
64 P. Singh, V. Srivastava and M. A. Quraishi, *J. Mol. Liq.*, 2016, **216**, 164–173.
65 M. S. Abusaif, A. M. Hyba, M. H. Helal, Y. A. Ammar, D. S. Aboul-Magd and A. Ragab, *J. Ind. Eng. Chem.*, 2025, DOI: 10.1016/j.jiec.2025.07.009.
66 A. Ragab, R. R. Raslan, M. S. Abusaif, H. K. Thabet, Y. A. Ammar and N. A. Gohar, *Eur. J. Med. Chem.*, 2025, 117751.
67 Y. M. Abdel-Baky, A. Ragab, M. S. Abusaif, Y. A. Ammar and A. M. Omer, *Carbohydr. Polym.*, 2025, 124049.
68 X. Ma, Y. Ma, L. Dong, X. Chang, T. Yang, X. Cao, L. Feng, Z. Hu and T. Hu, *Inorg. Chem. Commun.*, 2025, **175**, 114167.
69 K. D. H. Nguyen, T. D. Manh, L. T. P. Nguyen, D. T. Vu and K. L. D. Ngo, *J. Ind. Eng. Chem.*, 2025, **143**, 468–487.
70 Y. Liu, *Colloids Surf., A*, 2006, **274**, 34–36.
71 G. Nechifor, D.-E. Pascu, M. Pascu, G. A. Traistaru and P. C. Albu, *Sci. Bull. B*, 2015, **77**, 63–72.
72 A. A. El-Awady, B. A. Abd-El-Nabey and S. G. Aziz, *J. Electrochem. Soc.*, 1992, **139**, 2149.
73 C. G. Vaszilcsin, M. V Putz, A. Kellenberger and M. L. Dan, *J. Mol. Struct.*, 2023, **1286**, 135643.
74 M. M. Omran, M. M. Kamal, Y. A. Ammar, M. S. Abusaif, M. M. F. Ismail and H. H. Mansour, *Sci. Rep.*, 2024, **14**, 19818.
75 Y. Boughoues, M. Benamira, L. Messaadia and N. Ribouh, *Colloids Surf., A*, 2020, **593**, 124610.
76 R. Kaczmarczyk and S. Gurgul, *Energies*, 2024, **17**, 3223.
77 H. Lgaz, S. K. Saha, A. Chaouiki, K. S. Bhat, R. Salghi, P. Banerjee, I. H. Ali, M. I. Khan and I.-M. Chung, *Constr. Build. Mater.*, 2020, **233**, 117320.
78 R. S. Abdullah, N. A. Barghout, S. S. A. El-Sakka, M. H. Soliman, M. A. El-Hashash, S. Ragab and A. El Nemr, *Sci. Rep.*, 2022, **12**, 15484.
79 M. S. Abusaif, A. Ragab, E. A. Fayed, Y. A. Ammar, A. M. H. Gowifel, S. O. Hassanin, G. E. Ahmed and N. A. Gohar, *Bioorg. Chem.*, 2025, **154**, 108023.
80 M. S. A. El-Gaby, Y. A. Ammar, M. A. Ismail, A. Ragab and M. S. Abusaif, *Heterocycl. Commun.*, 2023, **29**, 20220170.
81 A. Ragab, D. M. Elsisi, E. M. Elqady, E. EL-Said, M. A. Salem, Y. A. Ammar and M. S. Abusaif, *Pestic. Biochem. Physiol.*, 2024, **202**, 105943.
82 M. M. F. Ismail, T. Z. Shawer, R. S. Ibrahim, M. S. Abusaif, M. M. Kamal, R. M. Allam and Y. A. Ammar, *RSC Adv.*, 2023, **13**, 31908–31924.
83 R. Oukhrib, Y. Abdellaoui, A. Berisha, H. Abou Oualid, J. Halili, K. Jusufi, M. Ait El Had, H. Bourzi, S. El Issami and F. A. Asmary, *Sci. Rep.*, 2021, **11**, 3771.
84 A. Ragab, M. A. Salem, Y. A. Ammar, W. M. Aboulthana, M. H. Helal and M. S. Abusaif, *Drug Dev. Res.*, 2024, **85**, e22216.
85 A. A. Ali, H. Abd El-Wahab, M. S. Abusaif, A. Ragab, O. A. Abdel-Jaid, E. A. Eldeeb and Y. A. Ammar, *Pigment Resin Technol.*, 2024, **53**, 557–568.
86 A. Gangan, A. Fahmy, S. A. Shaban and Z. M. El-Bahy, *Adv. Compos. Hybrid Mater.*, 2025, **8**, 178.
87 H. Senbill, A. Gangan, A. M. Saeed, M. E. Gad, J. Zeb and A. Fahmy, *Sci. Rep.*, 2025, **15**, 3334.